Comparisons of Instantaneous TRMM Ground Validation and Satellite Rain Rate Estimates at Different Spatial Scales

David B. Wolff[1,2] and Brad L. Fisher[1,2]
[1]*Science Systems & Applications, Inc, Lanham, Maryland*
[2]*NASA Goddard Space Flight Center, Greenbelt, Maryland*

Popular Summary

NASA's Tropical Rainfall Measuring Mission (TRMM) was launched in November 1997. This mission was designed to study the global hydrological cycle and to better understand the role of clouds and precipitation in climate change. TRMM collects rainfall information using two different remote sensors on board the satellite – the TRMM microwave imager (TMI) and the Precipitation Radar (PR) – that measure surface rain rates in two distinctly different ways. Three instantaneous and monthly rainfall estimates are derived from these two data sources, using three different rain algorithms, one for the TMI, one from the PR and one that combines data (COM) from both the TMI and the PR. These three rain estimates are not generally in perfect agreement. It is therefore important to understand how they differ and why, and to determine for various climatic regimes, which algorithm performs better, and under what circumstances. In order to make such comparisons it is also important to link these space-borne measurements of rainfall with measurements of rainfall collected at the earth's surface. The primary purpose of this study was to inter-compare the three "instantaneous" satellite products for several different climatic regions using ground-based rain estimates determined from surface weather radars as an empirical reference. The ground estimates for this study used data from three Ground Validation (GV) sites established prior to the launch of TRMM: Melbourne, Florida; Houston, Texas; and Kwajalein Atoll, in the central Pacific Ocean.

The main study was divided into two parts and included all available satellite and GV data from 1999 to 2004. In the first part, instantaneous rain rates from the four rain products were averaged and matched in time and space within a 0.5° x 0.5° grid, while in the second part, the rain rates were matched at the base resolution of the TMI "footprint" (~150 km^2) which is quite large relative to base resolution or the PR, COM and GV. For the second part of the study, matching PR, COM, and GV rain rates were averaged inside of the TMI footprint (note there about eight PR and thirty-eight GV pixels fit inside of a single TMI footprint). Both analyses showed good agreement, with the four estimates generally found within 10-15% of each other, but there were some important exceptions, most notably during heavy rain events, when rain rates exceeded 20 mm hr^{-1}. This result suggested that one or more of the rain algorithms was either misinterpreting the rain information or the actual observation was providing incorrect information to the algorithm. A preferred mode of precipitation was also observed for TMI at rain rates near 2 mm hr^{-1} over the ocean, which was not evident in any of the other estimates. At high rain rates, the COM appeared to perform the best in direct comparisons with GV. The results showed that significant improvements in TRMM satellite rain estimates have been made since the launch of the satellite, but that more work needs to be done to better understand and correct differences between the various algorithms.

Comparisons of Instantaneous TRMM Ground Validation and Satellite Rain Rate Estimates at Different Spatial Scales

David B. Wolff[1,2] and Brad L. Fisher[1,2]

[1]Science Systems & Applications, Inc, Lanham, Maryland

[2]NASA Goddard Space Flight Center, Greenbelt, Maryland

Corresponding Author's Address:
David B. Wolff
NASA/GSFC, Code 613.1, Greenbelt, MD 20771
wolff@radar.gsfc.nasa.gov

Abstract

This study provides a comprehensive inter-comparison of instantaneous rain rates observed by the two rain sensors aboard the TRMM satellite with ground data from two regional sites established for long-term ground validation: Kwajalein Atoll and Melbourne, Florida. The satellite rain algorithms utilize remote observations of precipitation collected by the TRMM microwave imager (TMI) and the Precipitation Radar (PR) aboard the TRMM satellite. Three standard Level II rain products are generated from operational applications of the TMI, PR and Combined (COM) rain algorithms using rain information collected from the TMI and the PR along the orbital track of the TRMM satellite.

In the first part of the study, 0.25 x 0.25 instantaneous rain rates obtained from the TRMM 3G68 product were analyzed and compared to instantaneous GV rain rates gridded at a scale of 0.5° x 0.5. In the second part of the study, TMI, PR, COM and GV rain rates were spatio-temporally matched and averaged at the scale of TMI footprint (~ 150 km^2). This study covered a six-year period 1999-2004 and consisted of over 50,000 footprints for each GV site.

In the first analysis our results showed that all of the respective rain rate estimates agree well, with some exceptions. The more salient differences were associated with heavy rain events in which one or more of the algorithms failed to properly retrieve these extreme events. Also, it appears that there is a preferred mode of precipitation for TMI rain rates at or near 2 mm hr^{-1} over the ocean. This mode was noted over ocean areas of Kwajalein and Melbourne and has been observed in TRMM tropical-global ocean areas as well.

1. **Introduction**

The Tropical Rainfall Measuring Mission's (TRMM) Ground Validation (GV) Program was established early in the pre-launch phase of the mission with the principal long-term goals of determining the accuracy of the satellite rainfall measurements and the systematic biases stemming from application of the rainfall algorithms. More specifically, the validation program was structured around two validation strategies: 1) determining the quantitative accuracy of the integrated monthly rainfall products at GV regional sites over large areas of about 500 km^2 using integrated ground measurements, and 2) inter-comparing/validating instantaneous satellite and GV rain rate statistics at spatio-temporal scales optimized to the various resolutions of the satellite and GV sensors (Simpson et al. 1988, Thiele 1988). This ~~current~~ study will address both parts of the validation problem, but will primarily be concerned with validating the instantaneous satellite rain products.

The GV program was originally designed around estimating the random variance of the TMI, PR and COM standard rain products on monthly scales over the regional GV sites. In the pre-launch phase of the satellite mission, instantaneous validation was still considered somewhat intractable because of statistical uncertainties stemming from the spatio-temporal measuring characteristics of the satellite and GV observations. Direct instantaneous comparisons between coincident measurements are difficult to achieve without a sufficient number of regional overpasses. But empirically verifying the accuracy on monthly time scales using independent data sets at the surface has also posed logistical challenges due to the existence of temporal sampling errors in the integrated rain estimates.

The TRMM satellite retrieves rain information between 37 N and 37 S while orbiting over the surface of the earth. The satellite collects between one and three estimates per day over any given location within its sampling domain depending on the latitude of the orbit. Monthly rain estimates on regional scales are subsequently determined statistically from the mean rain rate inferred from all the observations collected in a given month at the resolution of the gridded Level III rain products. This sampling strategy results in a statistical mixing of the sampling and retrieval errors in the integrated rainfall products (Bell T. L. and P. K. Kundu 2000, Bell et al. 2001, Fisher 2007).

Various studies have shown that the sampling errors explain at least 8 to 12% of the variance between monthly satellite and GV rain estimates (Laughlin 1981, Shin and North 1988, Bell et al. 1990, Oki and Sumi 1994 and Fisher 2004, 2007). This significant contribution to the total error budget at monthly scales complicates determination of the accuracy of the satellite rain algorithms, since the connection between the instantaneous measurement and the rain estimate is to some extent lost in the statistical integration.

This study uses six years (1999-2004) of satellite overpasses of the GV site for comparison with coincident TRMM rain intensity estimates. The data is pixel-matched in both time and space and statistics are provided comparing GV rain intensities (derived via ground-based radars and rain gauges) to the three principal estimates from the TRMM satellite (PR, TMI and COM algorithms). The matching is performed on both a gridded product (3G68, 0.5° x 0.5°) and on the TMI footprint scale (~150 km^2). By performing these comparisons on an instantaneous scale, we are able to remove a large source of uncertainty in the satellite estimates.

2. Data Sources

a. TRMM GV

The GV program operationally produces quality-controlled rainfall products for four primary sites: Darwin, Australia (DARW); Houston, Texas (HSTN); Kwajalein, Republic of the Marshall Islands (KWAJ); and, Melbourne, Florida (MELB). These sites were established during the pre-mission phase of TRMM, providing researchers with a quasi-continuous, long-term time series of rainfall measurements at a higher spatio-temporal resolution than can be observed with the satellite sensors alone. The GV data subsequently provides an empirical surface reference for independently verifying the accuracy of TRMM measurements of rainfall (Thiele 1988).

The GV program is documented in Wolff et al. (2005), including site and product descriptions, as well as algorithms and data processing techniques. For this study, we used the TRMM 2A-53 instantaneous rain maps that are distributed to the scientific community through the Goddard Earth Sciences Data and Information Services Center (GES-DISC). The 2A-53 data provides instantaneous rain rates at a resolution of 2 km x 2 km and covers a continuous region extending 150 km from the given GV radar. Each rain map thus consists of a 151 x 151 pixel grid with the GV radar located at the center pixel.

Geographical maps of the gauge and radar networks at DARW, HSTN, KWAJ, and MELB are provided in Fig. 1. The maps in Fig. 1 illustrate one of the key operational dilemmas of TRMM GV. Namely, that principally ocean sites, such as KWAJ, that provide the most physically robust comparisons for passive microwave (PM) retrievals, provide only limited real estate for deployment of gauges that can be used for calibration and validation of the GV radar rainfall estimates. On the other hand, sites with substantial gauge coverage such as DARW, HSTN and MELB, lack extensive ocean coverage and contain significant coastal areas over which it is inherently difficult, if not impossible, for PM algorithms to robustly estimate rain intensities. Although it is well known that there are problems with current PM physical algorithms in coastal areas, we will show that the full-GV-area probability distributions of rain rates are dominantly affected by coastal algorithm uncertainties, and comparison to or validation of TRMM estimates without removing estimates near coastlines are doomed to failure, or at the very least, misinterpretation.

Figure 2 provides another depiction of the GV sites, illustrating the land/coast/ocean 1/6th degree terrain mask used by the Version 6 TMI algorithm to delineate geographical type: dark gray is "ocean", medium gray denotes "coast" (both coastal land and coastal water), and light gray denotes "land". Also shown are the more subjectively classified terrain types within each of the 0.5° grid locations of the TRMM 3G68 product, employed in this study. In these figures, "L" is for land, "C" for coast and "O" for ocean. Additionally, a GV coverage notation is provided ("F" for full coverage, and "P" for partial). The purpose of the coverage flag is to identify pixels that are both fully observed by the GV radar (i.e. ranges between 15 and 150 km), and that contain a super-majority of one geographical type (i.e. mostly ocean, coast or land, subjectively set at about 60%). For this study only "F" pixels were considered.

b. TRMM Satellite: TMI and PR rain sensors

The TRMM satellite was launched on 27 November 1997 into a sun asynchronous, low-earth orbit at an altitude of 350 km. In August 2001, the satellite was repositioned from an average altitude of 350 km to 402 km. This orbital adjustment was made in order to conserve fuel and to extend the life of the mission. Global analysis of instantaneous TMI and PR rain rates indicate that the boost only had a marginal affect on the TMI rain rates, but on average, PR rain rates appear to have been lowered. Systematic changes in the PR rain rates due to boost are still being investigated (J. Kwiatkowski, NASA GSFC 2006 personal communication).

The satellite instrument package described by Kummerow et al. (1998) includes a dual-complement of passive and active rain sensors – the TRMM Microwave Imager (TMI) and the Precipitation Radar (PR) – that collect rain information using different remote sensing techniques. The TMI passively collects rain information using nine channels at five microwave frequencies: 10.7, 19.4, 21.3, 37.0 and 85.5 GHz. The 21.3 GHz is the only channel that is not dually polarized (only the vertical channel is available at 21.3 GHz). The PR is the first space-borne radar used in the collection of rain observations. The PR operates at a frequency of 13.8 GHz and has a minimum sensitivity of about 17 dBZ (~0.25 mm hr^{-1}). The PR's horizontal and vertical resolutions near nadir are about 4.3 km and 250 m, respectively. Its superior vertical and horizontal resolution allows the PR to observe smaller scale precipitation features that cannot be unambiguously resolved by the TMI (Kummerow et al. 1998).

At 13.8 GHz (2.17 cm wavelength), the PR is strongly attenuated by intervening rain. To account for this reduction in the observed return signal, a path attenuation correction is applied to the measured reflectivity using the surface reference technique

(SRT). This methodology generates an effective reflectivity factor that is used in the subsequent estimation of surface and near-surface rain rates (Iguchi et al. 2000; Meneghini et al. 2000). The SRT naturally constrains the PR field of view (FOV) to a narrow cross-track swath of 250 km (i.e., cross-track scanning angles within 17° of nadir). The attenuation correction can be a significant source of error in heavy rainfall.

c. TMI rain algorithm with respect to ocean, land, coast classification

A detailed description of the specifics of the algorithms of the various TRMM estimates is beyond the scope of this paper, but are well described in the references above; however, it is important to note that distinct and important physical differences exist between the land, coastal and ocean retrievals for the various estimates. While there are inherent differences in the actual distribution of rainfall over land and ocean, much of the intra-satellite variance between the TRMM estimates over ocean and land is due to the physical assumptions and intrinsic uncertainties of the retrieval algorithms.

The Goddard Profiling (GPROF) algorithm estimates instantaneous TMI rain rates over the ocean, land and coast using precipitation information obtained remotely from the observed emissions and scattering of hydrometeors in the atmosphere. The information collected in all nine channels represents a radiometric temperature sounding at different depths of the precipitating cloud (Kummerow et al. 1998). To estimate the cloud liquid water content, the rain signal needs to be distinguished from the microwave background upwelling from the surface. This is most easily accomplished over the radiometrically cold oceans, which cover three-quarters of the earth's surface. Over the oceans, GPROF applies a physical algorithm utilizing the radiometric information of all nine TMI channels (Kummerow et al. 1996, Kummerow et al. 2001). The algorithm first applies a radiation transfer model to compute an observed brightness temperature profile from the rain information in each of the channels. The observed brightness temperature profile is next compared to a large database of cloud radiation model simulations, which locates the simulated cloud profile that results in the best match (Tau, et al. 1993, Olson et al. 2006). The algorithm then employs a simple inversion methodology using Bayes probabilistic theorem to determine the rain rate profile, R, given a brightness temperature profile Tb:

$$\Pr(\boldsymbol{R} \mid \boldsymbol{Tb}) = \Pr(\boldsymbol{R}) + \Pr(\boldsymbol{Tb} \mid \boldsymbol{R}) \qquad (1)$$

where Pr(R) is the probability that a certain profile R will be observed , and Pr(Tb| R) is the probability of observing the brightness temperature vector Tb.

The rain retrievals are considerably more complicated over the radiometrically warm land surface due to variations in soil moisture, vegetation and transpiration, and surface roughness and topography. So far, the difficulty in handling the microwave background over land has precluded the usage of the lower frequency emission channels. Spencer et al. (1989) showed that at 85.5 GHz a reduction in the detected signal related to the scattering of radiation from frozen hydrometeors above the freezing level can be used as an empirical estimator of rain rate. Rain rates over land are subsequently determined empirically from the scattering information in the two 85.5 GHz channels (Spencer 1989, Ferraro 1997, Conner and Petty 1998, McCollum and Ferraro 2003). However, brightness temperature-rain rate relations are not directly related to surface rainfall, since they characterize scattering processes in the higher regions of the cloud (Wilheit et al 2003). Currently, GPROF applies an empirically based rain algorithm originally developed by

Ferraro (1997) and McCollum and Ferraro (2003).

The problems over land are further exacerbated around coastal regions due to the sharp contrast between land and ocean surfaces of the TMI footprint. In this case, the radiometrically warm land and cold ocean surfaces are both present in the TMI footprint. Coastal pixels are treated using a decision tree that first determines whether rain exists in the pixel. If a determination of rain existence cannot be made then the pixel is classified as ambiguous and a rain rate is not assigned. If rain exists, then the rain rate is determined using empirical relations described in Huffman and Adler (1993) and McCollum and Ferraro (2005).

d. TMI, PR, COM datasets

For this study, we used two different data sets for comparison. The first, a gridded product known as 3G68 provides area rain averages in 0.5° x 0.5° latituded/longitude boxes for the TMI, PR and COM algorithms. For the second set of comparisons, we utilized the TRMM Level II footprint data obtained from the satellite-coincidence subsets of 2A12 (TMI), 2A25 (PR), and COM (2B31) products, and then calculated all of statistics at the scale of each individual footprint observed by the TMI that was within PR- and GV-viewable range of the respective GV site.

Table 1 provides the percentage of "land," "coast" and "ocean" areas for different geographical regions, along with the four primary TRMM GV sites. The "TRMM" area is defined from 35° N to 35° S latitude and represents the satellite's sampling domain, while the "Deep Tropics", a sub-set of this region, is defined between 10° N and 10° S latitude. Table 1 shows that all of the GV sites listed, except KWAJ, contain significant coastal areas; the rain rates inferred for the pixels classified as coast have the greatest amount of uncertainty, for reasons that were described previously. For brevity, we will provide detailed comparisons of our GV estimates over KWAJ and MELB.

KWAJ is essentially open ocean site and most suitable for validating the TMI ocean estimates in which all the rain information from the nine TMI channels are utilized. MELB, in contrast, is located in the sub-tropics and has a rain climatology that is dominated isolated convection and tropical cyclones. As can be seen in Table 1, MELB has a good distribution of land, sea and coastal pixels.

3. Comparisons of 0.5° x 0.5° gridded data

In Section 3a, TMI, PR and COM rain rates are inter-compared on monthly, annual and five-year time periods at a grid resolution of 0.5° x 0.5° to GV rain rates over the GV sites of KWAJ and MELB. PDFs of the instantaneous are then constructed in Section 3b using all of the data collected over five years for each of the four estimates.

The TMI, PR and COM rain rates were obtained from the 3G68 instantaneous rain product. This special satellite rain product provides instantaneous, area-averaged rain rates for the TMI, PR and COM along the orbital track of the TRMM satellite at a grid resolution of 0.5° x 0.5° (Stocker et al. 2001). For this grid spacing, satellite and GV rain rates were matched in both time and space, which effectively mitigated the temporal sampling errors as a source of uncertainty with respect to the non-contiguous sampling of the TRMM satellite. GV 0.5° x 0.5° gridded rain rates were subsequently obtaining by averaging the rain rates obtained during TRMM overpasses from the gridded 2A53 product described in Section 2.

To provide a more detailed comparison, the data from MELB was further subdivided into land, coast and ocean categories as defined by the TMI terrain mask (see Fig. 2). We note that only pixels with a coverage type of "Full" (F) were used, and thus the sub-sets consisted of all pixels designated as either FO (Full Ocean), FC (Full Coast) and FL (Full Land) types. For KWAJ, there are no land or coast pixels: for algorithmic purposes, it is treated as solely oceanic. However, the Version 5 TRMM algorithms considered KWAJ as nearly 40% coast, given the coarse surface-type mask (0.25°) used at that time. The finer resolution Version 6 TMI surface mask of ~0.166° was also manually modified to exclude classification of small islands and atolls as coastal, prior to implementation of the V6 algorithm (Olson et al. 2006). In this analysis, all GV rain maps (2A-53) from 1999-2004 were used for comparison to the TRMM estimates.

a. Comparison of monthly means of instantaneous rain rates

Figures 3-6 display the mean monthly area rain rates at KWAJ and MELB for each rain rate product (TMI, PR, COM and GV) over the period from 1999 to 2004. Table 3 lists the mean rain rates on annual and six-year time periods; the last three columns of the table report the associated biases for each of the satellite rain rates relative to GV.

The biases in Table 2 are defined via equation (2) using the mean GV rain rate as empirical reference:

$$Bias = \frac{\left(\overline{E} - \overline{G}\right)}{\overline{G}} \qquad (2),$$

where $\overline{E}$ is the mean rain rate of the satellite estimate (PR, TMI or COM), and $\overline{G}$ is the mean rate from GV.

The TMI, PR and COM FO estimates for KWAJ are shown in Fig. 3 and are seen to be in good agreement with GV, with a few notable exceptions observed during August 2000, May-June 2003, and several months in 2004. Refer to Table 2 for specific values of the annual means and the resultant biases. It is observed that the biases reported in Table 2 for KWAJ are predominantly negative. The five-year satellite-inferred rain biases were -13.7% (PR), -7.9% (TMI) and -5.7% (COM).

The negative satellite biases at KWAJ are attributed to two systematic sources of error: 1) known calibration issues in the GV radar at KWAJ and 2) an underestimation of the higher rain rates by the satellite algorithms (> 20 mm/hr). The variations in the calibration of the KWAJ radar are considered the largest contributor to the monthly biases reported in Table 2. The calibration issues related to the performance of the KWAJ radar are reported by Houze et al., (2004) Silberstein et al. 2005, and Marks et al. 2005. Houze et al. (2004) and Marks et al. (2005) identified sudden changes in the radar's calibration and related them directly to mechanical and engineering issues (e.g., replacement of parts) that arose during the study period. These calibration offsets were not taken into account in the v5 2A53 rain products. In conjunction with ongoing research and development at the TSVO, Silberstein et al. (2005) have developed and tested a new methodology for correcting these problems, known as the Relative Calibration Adjustment (RCA). The RCA uses a large sample of points in the radar's clutter field to both identify when calibration changes occur and determine the magnitude of the change; the methodology is currently undergoing final testing at the TSVO for use in the generation of the v7 2A53 products.

The systematic underestimation of the higher rain rates by the TMI and PR, in the case of KWAJ, is not as significant as the calibration offsets, but also contributes to the negative biases observed in Table 2. Moreover, an underestimation of rain rates at the high end of the rain rate spectrum was also observed in the case of MELB where the calibration has been stable over time. The algorithm issues associated with the determination of higher rain rates by the TMI and PR for KWAJ and MELB will be investigated in more detail in Section 4 in conjunction with the footprint analysis of the instantaneous rain rates.

For MELB, the data was stratified into ocean (FO), land (FL) and coast (FC) categories. The monthly rain rates for each case are displayed in Figs. 3, 4 and 5, respectively. The FO satellite and GV mean monthly rain rates shown in Fig. 3 exhibit good agreement but there are some notable disagreements, especially during peak rainfall months. In Table 2, the PR annual bias, relative to GV, is positive in five out of six years while the COM is positive in all six years. The TMI FO biases, on the other hand, are negative for each of the six years. In general, the peak rainfall months contribute the bulk of the annual biases shown in Table 2.

In contrast with the FO case, the PR bias over coast and land is predominantly negative. The TMI land bias, on the other hand, is more variable, and was positive in four out of six years, whereas it was negative for all six years in the ocean case. This observation is also consistent with the overall six-year biases, which in the FL case was +10.2 and -8.1 in the FO case. Over the coast, the TMI FC bias tended to be negative, but with year-to-year results covering a broad range between -34.9 and +18.5 over the six-year study period. These results pointedly reflect the differences in the TMI algorithm for about 0.6 mm hr^{-1}.

Figure 8 provides the ensemble PDF and CDF at MELB for ocean (FO), coast (FC) and land (FL) pixels, in the left, middle and right hand panels, respectively. Over ocean, the CDF agree quite well, with median rain rates differing by less than 1 mm hr^{-1}. Over coastal pixels, the scatter among the CDFs is more evident, showing better agreement between the PR and TMI estimates, which are both lower than the GV and COM estimates. In general, the GV distributions fall within the bounds of the other distributions. Over land, there is better agreement between the estimates than over coast. Also, over land, the PR rain rates are less than the other estimates, while the TMI and GV rates are quite similar.

In summary, our 0.5° gridded comparisons the data show that there is good agreement between the various estimates, and that there are no systematic biases shown between one estimate versus the other. The discrepancies that do occur are associated with specific (heavy) precipitation events; however, overall the near decade-long TRMM products, and the GV estimates to which they are compared, are quite robust and provide a unique dataset for future study of precipitation physics and climate analyses.

4. Validation at the TMI Footprint Scale

a. Description of analysis

The original emphasis of the GV validation program was on verifying the accuracy of the Level III monthly products at planned GV sites using well-calibrated rain surface-based rains sensors. The primary goal was to characterize the errors in the satellite rain products used in climate-scale applications at an averaging scale that minimized the space-time uncertainties between surface and satellite sensors (Thiele 1988). In addition to the obvious interest in quantifying the error bounds in the higher-level TRMM products, there was also interest in using the GV data to assess the accuracy of the TRMM Level II instantaneous rain products at the fundamental resolution of the satellite sensors (i.e. the footprint scale), for instantaneous validation provides a more direct physical probe of the systematic errors in the operational rain algorithms.

Validation at instantaneous scales, perhaps most importantly, eliminates the temporal sampling error from consideration. Previous studies of the temporal sampling error – the error associated with the discreet regional sampling of the satellite – have shown that it can account for up to 25% of the variance between satellite and ground estimates on monthly scales (Laughlin 1981, Oki et al. 1994, Fisher 2004, Fisher 2007). But even given coincident, instantaneous observations on larger scales (e.g., TRMM 3G68), small-scale discrepancies between satellite rain products due to inter-algorithmic differences can become "smoothed out" in the averaging process, limiting the usefulness of such comparisons. Random errors, however, increase substantially as the time-space averaging scale is reduced to the footprint scale, due to navigational uncertainties between GV and satellite and differences in the measuring characteristics of the sensors.

In this part of the study, Level II TMI, PR, and COM instantaneous rain rates were matched at the scale of the TMI footprint and were statistically compared to the Level 2A53 GV radar rain rate spectrums at both KWAJ and MELB. Six years of regional TRMM overpass data were used (1999-2004). As seen in Table 3, the available data provided a large sample of more than 50,000 TMI footprints for each GV site, with each TMI footprint covering an area of about 150 km^2. Though the TMI "footprint" used in this study provides a convenient scale for analysis, it should not be thought of as representing a fundamental physical scale, because it results from an empirical optimization of rain information that contains rain information spanning a broad physical spectrum of scales (Olson et al. 2006). The effective field of view at 10 GHz, for example, is 67 x 37 km^2, whereas at 85 GHz the field of view is 7 x 5 km^2 (the Level II TMI footprint, in effect, under-samples the low frequency channels and over-samples the high frequency channels).

The swaths of the TMI and the PR sensors along TRMM's orbital track represent the sampling domain of the satellite. The GV sampling domain of the radar encompasses a circular domain extending 150 km from the radar location. For this analysis, the instantaneous rain rate information was restricted to the geographical intersection of the TMI and PR orbital track within the GV radar domain. Figure 9 displays four instantaneous snapshots for the GV, TMI, PR and COM, rain rate estimates for TRMM Orbit #01707 on 10/07/1999 over KWAJ, in the top-left, top-right, bottom-left and bottom-right panels, respectively. These images illustrate the rain rates at the characteristic or native resolution of each of the respective estimates. The red and blue dashed lines illustrate the edges of the orbital track of the PR.

To simplify the procedure, we matched the TMI, PR and COM and GV at the scale of the TMI footprint by considering a 7 km radius around the center of the TMI pixel location. Unconditional mean rain rates (i.e., $R \geq 0$) were then computed for the GV, PR, and COM at the TMI footprint scale by locating all of the pixels (rainy and non-rainy) found within this circular region. Figure 10 illustrates the same instantaneous snapshots as Fig. 9, but after the GV, PR and COM rain rates were averaged within the respective TMI footprint areas.

The number of GV, PR and COM pixels associated with each TMI footprint vary from case to case, but tend to average about 8 for the PR and COM (native resolution of ~4.3 km x 4.3 km $\cong$ 18.5 km^2 resolution) and about 36 for the GV (native resolution of 2 km x 2 km = 4 km^2 resolution). The TMI surface flag was also recorded for each set of matching pixels according to whether the TMI pixel was labeled ocean, land or coast, as described previously. Table 3 gives a summary of the number of overpasses and the number of footprints for each of the four GV locations and lists both the total number of footprints and number of footprints in each terrain category (O, L, C) used in this analysis.

Footprint statistics: mean rain rate profiles

Using the GV matching rain rates as an empirical reference, mean rain rate profiles were generated for the TMI, PR and COM spanning a dynamic range between 0 and 40 mm·hr^{-1}. The profiles were constructed by first binning the instantaneous rain rates matched at each TMI pixel for all four products at 1 mm·hr^{-1}intervals with respect to the GV rain rate. For example, if the GV rain rate for a given TMI pixel was 5.5 mm hr^{-1} the TMI, PR and COM rain rates were included in the 5 to 6 mm hr^{-1} bin. The data in each separate bin was then averaged, after which a 3 mm·hr^{-1} (± 1 mm·hr^{-1}) mean filter was applied across the entire spectrum. The application of a mean filter was mainly required to increase the effective sample sizes in the higher bins (> 20 mm·hr^{-1}).

Figures 11 and 12 show mean rain rate profiles constructed for KWAJ and MELB, respectively. In Fig. 12, for MELB, in addition to plotting a mean profile for all the data combined (top left), three additional profiles are shown that subdivide the data according to the TMI terrain surface flag (O, L, or C).

The rain rate profiles shown in Figs. 11 and 12 are represented as scatter diagrams, but it should be noted that the satellite estimates are being validated against the GV profile. The GV profile, by definition, has a slope of one. The satellite rain rate information in turn was sorted with respect to the GV profile before performing any regressions.

A regression analysis was subsequently carried out on each of the profiles shown in Figs. 11 and 12 by splitting the rain rate spectrum into two equal sectors, designated as high and low rain rate regimes. The "low" and "high" regimes were defined from 0 to 20 mm·hr^{-1} and from 21 to 40 mm hr^{-1}, respectively. The regression parameters listed in

Tables 4 and 5 will be referred to in the following analysis to help illustrate differences between the two parts of the spectrum.

In general, Figs. 11 and 12 for KWAJ and MELB show good correspondence between the TMI, PR and COM with GV, in the lower regions of the rain rate spectrum. The correspondence is considerably less in the higher region of the spectrum, with the COM showing the best agreement with respect to GV. Although the higher rain rates represent an important region of the spectrum – because of their association with convective rain processes – the sample sizes in each bin are considerably smaller, and thus to some extent lessoning their contribution to the total integrated rainfall. Of course, since the data was spatially averaged at the scale of the TMI footprint, it is not surprising that there are significantly fewer rain rate samples in the high regime in the cases of the PR and COM (> 20 mm·hr^{-1}).

In the lower rain rate regime, the linear correlation coefficients between GV and satellite rain products seen in Tables 4 and 5 are seen to be consistently high ($\rho \geq .95$) for both KWAJ and MELB. In the high rain rate regime, the correlations drop off substantially with large non-zero intercepts along with lower slope values. Even in the low regime, the slopes of each satellite profile reveal systematic differences in the mean rain rate statistics that lend some explanation for the observed biases in Table 2. Further examination of Figs. 11 and 12 also show greater variance between the three satellite estimates. It is subsequently in the high rain rate regimes where the differences between the rainfall algorithms are most apparent. With respect to GV, the COM rain rate profile shows the best overall agreement across both high and low regimes. The PR and COM profiles interestingly appear quite similar in the ocean case for both KWAJ and MELB, but in the land and coast cases, the PR noticeably underestimates the higher rain rates relative to both GV and COM. This behavior dominates the overall profile for MELB shown in Fig. 12 (top left).

The TMI-GV rain rate profiles comparisons reveal the most discrepancies, especially in the high rain rate regime, and for all terrain categories. Even in the low regime, however, the TMI estimates trends distinctly lower with respect to the GV, PR and COM estimates. The low slope value observed in the high regime, which is evident in all the panels shown in Figs. 11 and 12, is attributed to the saturation of the TMI signal in the lower channels. The highest TMI rain rates are observed in the land case, which in examination of Table 2 was the only case where the TMI showed an overall positive bias (+10.2). In every other case the overall bias was negative. In the MELB land case the determination of the TMI rain rate is empirically determined based on the high frequency 85 GHz channel and is not dependent on the physical saturation of the signal that naturally occurs in the lower channels.

In the TMI ocean case, mean rain rates rarely exceed 30 mm hr^{-1}. The saturation of the lower frequency TMI channels (10.7, 19.4, 21.3 GHz) was addressed in the original design of the TMI sensor. Based on prior experience with SSMI/I, the water vapor channel was shifted from 22.235 to 21.3 GHz to avoid saturating the signal, in which higher brightness temperatures in the 21.3 GHz channel are correlated with higher rain rates (Kummerow et al. 1998), but this sensor modification obviously did not eliminate the problem entirely and TMI ocean rain rates at both KWAJ and MELB revealed a negative bias of -8.8 and -9.2, respectively. Ha and North (1995), moreover, point out that above 20 mm hr^{-1} the scattering of microwave radiation becomes important the high rain rate regime at MELB, especially in the land and coast stratifications. These results for the COM are encouraging, but it should also be noted that in Table 2, the COM biases at MELB were consistently positive and absolute values exceeded both the TMI and PR. However, Figures 11 and 12 both suggest that significant improvements in rain estimation can be realized using information from both sensors, even when the individual sensors exhibit different rain characteristics.

b. *Footprint statistics: standard errors*

Satellite errors were estimated across the rain rate spectrum at 1 mm·hr^{-1} intervals by computing the relative variance, $\sigma_{err}^2(i)$, between the satellite and the GV mean rain rate for a given rain rate bin, using the following expression:

$$\sigma_{err}^2(i) = var(s_i - \bar{r}_i) = \sigma_s^2(i) + \sigma_r^2(i) - 2cov(s_i, \bar{r}_i). \qquad (3)$$

The standard error was then computed by taking the square root of the resulting error variance:

$$\sigma_{err}(i) = \sqrt{\mathrm{var}(s_i - \bar{r}_i)} \qquad (4)$$

In (3) and (4), s_i and $\bar{r}_i$ correspond to the satellite and GV rain rate for the ith rain rate bin as determined by GV. Note that σ_s and $2cov(s_i, \bar{r}_i)$ are the largest terms in (2), since the statistical distribution for $\bar{r}_i$, as represented by σ_r, is confined within a 1 mm·hr^{-1} interval as described in the previous section.

A 7-bin (± 3 mm·hr^{-1}) mean filter was applied at each point and error profiles were then generated for the TMI, PR and COM across a dynamic range of rain rates between 0 and 30 mm hr^{-1}. These standard error profiles for KWAJ and MELB are characteristics between 0 to 30 mm hr^{-1}, with estimated errors increasing monotonically from 0 to about 15 mm hr^{-1}. The algorithm-based method subsequently indicates that the TMI errors are spread over a broader range. The results of this study, of course, may contain some regional dependence at the higher rain rates. The TMI profiles for MELB and KWAJ, for example, are fairly similar in the lower range of rain rates below 20 mm hr^{-1}, but diverge above 20 mm hr^{-1}, with MELB exhibiting more sharply increasing errors relative to KWAJ. More analysis will be required to verify these inferred error characteristics.

c. Probability distributions at the TMI footprint scale.

i. KWAJ

Figure 16 provides the rain rate PDF and CDF for each estimate at the footprint level at KWAJ. Also, shown are the resultant mean rain rates (2.01, 1.59, 1.83 and 1.61 for GV, PR, TMI and COM, respectively), as well as the total number of 'footprints' that were used for averaging the various estimates. Given the large number of points available for generating these distributions, much can be deemed by analysis of the individual PDFs. Most notably, note that the basic shapes of the GV, PR and COM distributions are quite similar, with rather flat unimodal peaks near 0.5 mm hr^{-1}; however, the TMI distributions is much more peaked with a pronounced mode at about 2 mm hr^{-1}.

Overall, the COM and PR CDFs agree the best, and the TMI estimates are considerably higher at all rain rates up to about the 90th percentile (just over 2 mm hr^{-1}). Again, as in Section 3, we see that the GV CDF falls within the bounds of the other CDFs. An interesting set of questions arises here as to why the TMI PDF is so dissimilar to the other PDFs? Is this due to land affects of the atoll on the TMI estimates (which the algorithm assumes do not exist), or is this an inherent issue with TMI PDFs over ocean? Others have shown some unusual characteristics of TMI oceanic PDFs. In a global study, Yuter et al. 2006 showed that there are preferred regions where TMI PDFs can be described as "physically implausible."

To determine whether the land areas of the atoll affected the TMI estimates, we sub-divided the KWAJ GV domain as illustrated in Fig. 17. In this figure, the shaded regions directly over KWAJ were designated as "coast" with the remainder of the areas (white region within 150 km from the radar) designated as "ocean." As mentioned previously, this rather crude mask, which was used in all TMI products prior to Version 6, was at 0.25° resolution. Any 0.25° pixel that contained land mass was assumed to be either coast or land (depending on the amount of land in the given pixel), and using this classification resulted in KWAJ being considered approximately 40% coast (for Version 5 algorithmic purposes). Note that the data used for this comparison were still from the Version 6 database, but the terrain classification was via Version 5 surface masking. Figure 18 shows the PDF of KWAJ rain rates for the various estimates. Ocean (V5-deemed ocean pixels), and coast (V5-deemed coastal pixels) in the left, middle and right hand panels, respectively. While the resultant means are slightly different, the distributions themselves are nearly indistinguishable, which seemingly negates the hypothesis that land affects caused the different behavior of the TMI PDF versus the PDF of the other estimates.

To investigate whether or not this is possibly due to an inherent issue in ocean TMI estimates, a dataset of distributions of TMI rain rates over 2.5° pixels throughout the tropics compiled by T. Bell (NASA GSFC 2006 *personal communication*) was utilized. Figure 19 shows an ensemble of monthly PDFs of TMI rain rates for the period 1999-2004, for ocean, land and coast, in the left-, middle- and right-panels, respectively. The ocean PDFs clearly show a preferred mode of about 2 mm hr^{-1}, as seen over KWAJ and MELB, indicating that there is indeed some algorithmic preference for such estimated rain rates. The land PDF shows the difficulty of estimating light rain rates, given the restrictions imposed by the sole use of ice scattering as a precipitation estimate. Also, the TMI-observable rain rates are significantly higher over land than over ocean. This fact is due to both actual differences in precipitation characteristics over land and ocean, and the failure of current TMI to estimate higher rain rates over ocean due to the saturation of the signal and beam-filling issues discussed previously.

ii. MELB

Fig. 20 provides the rain rate PDFs and CDFs from the various estimates at MELB for All, Ocean, Land, and Coast, in the top-left, top-right, lower-left and lower-right panels, respectively. What immediately stands out in the "All" PDF is the peaked TMI distribution of rates, with a mode at about 0.8 mm hr^{-1}, which differs significantly from all of the other PDFs. A quick examination of the "Coastal" PDF shows the dominant effect that coastal areas have on estimated rain rates for the TMI. However, over ocean and land, all of the estimates agree quite well, but there is indeed a noticeable 2 mm hr^{-1} TMI rain rate mode evident at MELB over ocean areas, as was also shown to exist at KWAJ and the tropical oceans in general. The erroneous mode is most probably due to the developers of the PR algorithm. An evaluation of the mean rain rate spectrum suggested that COM performed better at the higher rain rates relative to GV than either v6 TMI or v6 PR. But in some cases the COM errors were significantly higher, perhaps suggesting an inconsistent handling of the high rain rate cases. This result will need to be more closely examined in future work. Although more work needs to done, the results from the footprint part of the study are encouraging because it shows that statistically meaningful GV- satellite inter-comparisons can be performed at the spatio-temporal scale of the TMI footprint, provided there exists a sufficiently large sample of overpasses.

It was also shown that there is a preferred mode in the TMI rain rate distributions at approximately 2 mm hr^{-1} that was not evident in any of the other distributions, thus indicating that more work needs to be done to improve the over-ocean estimates by the TMI algorithm developers.

5. Acknowledgements

This work was funded by NASA Grant NNG07EJ50C. The authors would like to thank Dr. Ramesh Kakar (NASA Headquarters), Dr. Robert Adler (TRMM Project Scientist) and Mr. Richard Lawrence (Chief, TRMM Satellite Validation Office) for their support of this effort. We also appreciate the support staff of the TSVO, including David Makofski, Bart Kelley, David Marks, David Silberstein, and Jason Pippitt.

References

Amitai, E., X. Llort, and D., Sempere-Torres, 2006: *Opportunities and challenges for evaluating precipitation estimates during GPM mission.* Meteorlogische Zeitschrift, **15**, 551-557.

Bell, T., L., A. Abdullah, R. L. Martin and G. North, 1990: Sampling errors for satellite-derived tropical rainfall: Monte Carlo study using a space-time stochastic model. *J. Geophys. Res.*, **95**, 2195-2205.

Bell T. L., and P. K. Kundu, 2000: Dependence of satellite sampling error on monthly averaged rain rates: comparison of simple models and recent studies. *J. Appl. Meteor.*, **13**, 449-462.

Bell, T., L, P. K. Kundu, and C. D. Kummerow, 2001: Sampling errors of SSM/I and TRMM rainfall averages: Comparison with error estimates from surface data and a simple model. *J. Appl. Meteor.*, **40**, 938-954.

Conner M.D., and G. W. Petty, 1998: Validation and intercomparison of SSM/I rain-rate retrieval methods over the continental United States. *J. Appl. Meteor.*, **37**, 679-700.

Ferraro, R. R., 1997: Special sensor microwave imager derived global rainfall estimates for climatological applications. J. Geophys. Res., **102**, 16,715-16,735.

Fisher, B. L., 2007: Statistical error decomposition of regional-scale climatological precipitation estimates from the Tropical Rainfall Measuring Mission (TRMM). *J. Appl. Meteor. and Climatol.*, in press.

Fisher, B. L., 2004: Climatological validation of TRMM TMI and PR monthly rain products over Oklahoma. *J. Appl. Meteor.*, **43**, 519-535.

Ha E., and G. R. North, 1999: Error Analysis for some ground validation designs for satellite observations of precipitation. *J. Atmos. Oceanic Technol.*, **16**, 1949-1957.

Houze, R. A, S. Brodzik, C. Schumacher, S. E. Yuter, and C. R. Williams, 2004: Uncertainties in oceanic radar rain maps at Kwajalein and implications for satellite validation. *J. Appl. Meteor.*, **43**, 1114-1132.

Iguchi, T., T. Kozu, R. Meneghini, J. Awaka, K. Okamoto, 2000: Rain-profiling algorithm for the TRMM precipitation radar. *J. Appl. Meteor.*, **39**, 2038-2052.

Kummerow, C. W. Berg, J. Thomas-Stahle, and H. Masunaga, 2006: Quantifying global uncertainties in a simple microwave rainfall algorithm. *J. Atmos. Oceanic Technol.*, **23**, 23-36.

Kummerow, C., and Coauthors, 2001: The evolution of the Goddard profiling algorithm (GPROF) for rainfall estimation from passive microwave sensors. *J. Appl. Meteor.*, **40**, 1801-1820.

Kummerow, C. W. Barnes, T. Kozu, J. Shiue, J. Simpson, 1998: The tropical rainfall measuring mission (TRMM) sensor package. *J. Atmos. Oceanic Technol.*, **15**, 809-817.

Kummerow, C., 1998: Beamfilling errors in passive microwave rainfall retrievals. *J. Appl. Meteor.*, **37**, 356-369.

Kummerow, C. W., W. S. Olson, L. Giglio, 1996: A simplified scheme for obtaining precipitation and vertical hydrometeor profiles from passive microwave sensors. *IEEE Trans. Geo. Remote Sens.*, **34**, 1213-1232.

Laughlin, C. R., 1981: On the effect of temporal sampling on the observation of mean rainfall. *Precipitation Measurements from Space*, D. Atlas and O. Thiele, Eds., NASA Publication, D59-D66.

Marks, D.A., D.B. Wolff, D.S. Silberstein, J.L. Pippitt, and J. Wang, 2005: Improving radar rainfall estimates at Kwajalein Atoll, RMI through relative calibration adjustment, *Preprints, 32nd Conference on Radar Meteorology, 3R.1 AMS* Albuquerque, NM, October 24-29, 2005.

McCollum, J. R. and R. R. Ferraro, 2003: Next Generation of NOAA/NESDIS TMI, SSMI/I, and AMSR-E microwave land rainfall algorithms. *J. Geophys. Res.*, **108**,

McCollum, J. R. and R. R. Ferraro, 2005: Microwave rainfall estimation over coasts. *J. Atmos. and Oceanic Technol.* **22**, 497–512.

Meneghini, R., T. Iguchi, T. Kozu, L. Liao, K. Okamoto, J. A. Jones, J., Kwiatkowski, 2000: Use of the surface reference technique for path attenuation estimates from the TRMM precipitation radar. *J. Appl. Meteor.*, **39**, 2053-2070.

Oki, R., and A. Sumi, 1994: Sampling simulation of TRMM rainfall estimation using radar-AMeDAS composites. J Appl. Meteor., 33, 1597-1608.

Olson, W. S., and Co-authors, 2006: Precipitation and latent heating distributions from satellite passive microwave radiometry. Part I: Improved method and uncertainty estimates. *J. Appl. Meteor.*, 702-720.

Shin, K., and G. R. North, 1988: Sampling error study for rainfall estimate by satellite using a stochastic model. *J. Appl. Meteor.*, **27**,1218-1231.

Silberstein, D. S., D. B. Wolff, D. A. Marks, and J. L. Pippitt, 2005: Using ground clutter to adjust relative radar calibration at Kwajalein, RMI. *Preprints, 32nd Conference on Radar Meteorology, 3R.2, AMS*, Albuquerque, NM, October 24-29, 2005.

Simpson, J., R. F. Adler, G. R. North, 1988: A proposed tropical rainfall measuring mission (TRMM) satellite. *Bull. Amer. Meteor. Soc*, **69**, 278-294.

Spencer, R., W. H. Goodman, and R. E. Hood, 1989: Precipitation retrieval over land and ocean with the SSM/I: identification and characteristics of the scattering signal. *J. Appl. Meteor.*, **6**, 254-273.

E. F. Stocker, J. Kwiatkowski and O. Kelley. 2001. Gridded Hourly Text Products: A TRMM Data Reduction Approach. Proceedings of IEEE 2001 International Geoscience and Remote Sensing Symposium. Sydney, Australia. pp. 658-660.

Tao, W.-K., and J. Simpson, 1993: Goddard Cumulus Ensemble Model. Part I: Model description. *Terr. Atmos. Oceanic Sci.,* **4**, 35-72.

Thiele, O., 1988: Validating Space Observations of Rainfall. *Tropical Rainfall Measurements*, J. S. Theon and N. Fugono, Eds., A. Deepak Publishing, 415-423.

Wilheit, T. T., A. Chang, L. Chiu, 1991: Retrieval of monthly rainfall indices from microwave radiometric measurements using probability distribution function. *J. Atmos. Oceanic Technol.*, **8**, 118-136.

Wilheit, T., C. Kummerow and R. Ferraro, 2003: Rainfall algorithms for AMSR-E, *IEEE: Trans. Geoscience & Rem. Sensing*, **41**, 204-214.

Wolff, D. B., D. A. Marks, E. Amitai, D. S. Silberstein, B. L. Fisher, A. Tokay, J. Wang, and J. L. Pippitt, 2005: Ground validation for the Tropical Rainfall Measuring Mission (TRMM). *J. Atmos. Oceanic Technol.*, **22**, 365-380.

Yuter, S., M. Miller, J. Stout, R. Wood, J. Kwiatkowski, D. Horn, and C. Spooner, 2006: Remaining challenges in satellite precipitation estimation for the Tropical

Rainfall Measuring Mission. Preprints, 4th European Conference on Radar in Meteorology and Hydrology. 18-22 September 2006, Barcelona, Spain.

List of Figures

Fig. 7: Probability Density Function (PDF) and Cumulative Distribution Frequency (CDF) of instantaneous rain rates (0.5° resolution) for GV (solid), PR (dot), COM (dash-dot) and TMI (dash) as inferred from 3G68 products using 0.5° resolution for the period 1999-2004 at KWAJ.

Fig 8: Same as Fig. 7, except for MELB over ocean (left panel), coast (middle panel) and land (right panel).

Fig. 9: Illustration of a TRMM overpass of the KWAJ GV sites on 10/07/1999 showing the Level II rain data at each instrument's native resolution: top left panel (GV 2 km x 2 km; top right panel (TMI ~150 km^2 resolution); bottom left panel (PR 4 km at nadir); and bottom right panel (COM 4 km at nadir).

Fig. 10: Same as Fig. 9, except the GV, PR and COM data have been averaged within each TMI footprint.

Fig. 11: Scatter diagram of TMI (black), PR (blue) and COM (red) mean rain intensities versus mean rain intensities of the GV radar at Kwajalein.

Fig. 12: Scatter diagrams of TMI (black), PR (blue) and COM (red) mean rain intensities versus mean rain intensities of the GV radar at Melbourne. The four panels show rain

rate profiles for: (top left) all matched data points; (top right) Ocean only; (bottom left) Land only; (bottom right) Coast only.

Fig. 13: Scatter diagrams based on 150 good overpasses of GV site at Melbourne showing rain rate profiles for PR (version 5), PR (version 6) and COM.

Fig 14: Profile displays the standard errors for the TMI, PR and COM at KWAJ versus the GV rain rate intensity. Errors were determined based on the variance difference between the matched satellite rain rates and the GV radar at Kwajalein.

Fig. 15: Profile displays the standard errors for the TMI, PR and COM at MELB versus the GV rain rate intensity. The four panels show results for: (top left) all matched data points; (top right) Ocean only; (bottom left) Land only; (bottom right) Coast only.

Fig. 16: PDF and CDF of rain rates for GV (solid), PR (dot), COM (dash-dot) and TMI (dash) estimates using 0.5° resolution for the period 1999-2004 at KWAJ at the TMI footprint scale.

Fig. 17: Sub-setted classification of KWAJ using a rough estimate of the TMI Version 5 surface mask, which considered the areas near the atolls to be coastal.

Fig. 18: PDF and CDF rain rates at KWAJ over gray area shown in Fig. 17 (top left panel), white area in Fig. 17 (middle panel) and all areas (same as in Fig. 16).

Fig. 19: PDF of TMI rain rates over 2.5° x 2.5° boxes over ocean (top left), land (middle) and coast (right). Data are color-coded by month and year and the ensemble. The dashed red lines represent August, 2001, which corresponds to the period during the TRMM boost from 350 km to 402 km. Data displayed in figure was obtained from Dr. Thomas Bell (NASA GSFC).

Fig. 20: PDF and CDF of rain rates at MELB at the TMI footprint scale for the period 1999-2004 showing GV (solid), PR (dot), COM (dash-dot) and TMI (dash). Top left panel shows the full GV area; top right panel is for ocean areas only; bottom left panel is for land areas only, and the bottom right is for coastal areas only.

Table 1: The number of 1/6° pixels and percentages (in apostrophes) of geographical types, via the TRMM TMI Version 6 algorithm, as a function of sampling area: Global represents ± 70° latitude; TRMM area is ±35° latitude, Deep Tropics is ±10°. Also shown are the respective percentages of geo-types at the four GV sites. Note that all GV sites except KWAJ have significant z coastal area, limiting the usefulness of comparisons to passive microwave estimates.

Area	***Ocean***	***Land***	***Coast***	***Other***	***Total***
Global	952643 (40.8)	682813 (29.3)	154289 (6.6)	543055 (23.3)	2332800
TRMM	646298 (71.2)	217582 (24.0)	43044 (4.7)	276 (0.0)	907200
Deep Tropics	191754 (74.0)	51275 (19.8)	16171 (6.2)	~	259200
KWAJ	441 (100.0)	~	~	~	441
MELB	112 (41.5)	72 (26.7)	86 (31.9)	~	270
HSTN	90 (27.8)	153 (47.2)	81 (25.0)	~	324
DARW	104 (27.5)	104 (27.5)	170 (45.0)	~	378

Table 2: Statistics for 3G68 comparison for KWAJ and MELB showing site, year, mean rain rates (GV, PR, TMI and COM), as well as the GV-relative biases.

Site	Year	Type	GV Mean	PR Mean	TMI Mean	COM Mean	PR Bias	TMI Bias	COM Bias
MELB	1999	FL	0.1923	0.1806	0.2069	0.2239	-6.1	7.6	16.4
MELB	2000	FL	0.0838	0.068	0.0743	0.0822	-18.9	-11.3	-1.9
MELB	2001	FL	0.0971	0.093	0.0993	0.1175	-4.3	2.2	21.0
MELB	2002	FL	0.1814	0.1582	0.1766	0.2052	-12.8	-2.6	13.1
MELB	2003	FL	0.2194	0.2142	0.2778	0.2769	-2.4	26.6	26.2
MELB	2004	FL	0.1266	0.1228	0.1538	0.1592	-2.9	21.5	25.8
MELB	**1999-2004**	**FL**	**0.1516**	**0.1409**	**0.167**	**0.1795**	**-7.0**	**10.2**	**18.4**
MELB	1999	FC	0.1541	0.1426	0.1232	0.1705	-7.4	-20.0	10.7
MELB	2000	FC	0.1038	0.0817	0.0675	0.0956	-21.2	-34.9	-7.8
MELB	2001	FC	0.1256	0.1034	0.1054	0.1366	-17.7	-16.1	8.7
MELB	2002	FC	0.1542	0.1454	0.1412	0.181	-5.7	-8.4	17.4
MELB	2003	FC	0.1079	0.1106	0.1279	0.144	2.5	18.5	33.4
MELB	2004	FC	0.1135	0.1113	0.1136	0.1336	-1.9	0.1	17.7
MELB	**1999-2004**	**FC**	**0.1263**	**0.1161**	**0.1139**	**0.1439**	**-8.1**	**-9.9**	**13.9**
MELB	1999	FO	0.1369	0.1254	0.1164	0.1506	-8.4	-15	10.1
MELB	2000	FO	0.0873	0.089	0.0774	0.1046	2.0	-11.4	19.9
MELB	2001	FO	0.1199	0.1232	0.1118	0.1504	2.7	-6.8	25.4
MELB	2002	FO	0.13	0.1363	0.1194	0.164	4.9	-8.1	26.2
MELB	2003	FO	0.1098	0.1153	0.1071	0.1426	5.0	-2.5	29.8
MELB	2004	FO	0.0918	0.1115	0.087	0.1058	21.5	-5.1	15.4
MELB	**1999-2004**	**FO**	**0.1124**	**0.117**	**0.1032**	**0.1364**	**4.1**	**-8.2**	**21.3**
KWAJ	1999	FO	0.1651	0.1392	0.1459	0.1603	-15.7	-11.6	-2.9
KWAJ	2000	FO	0.2881	0.2571	0.2536	0.2817	-10.8	-12.0	-2.2
KWAJ	2001	FO	0.2149	0.1816	0.2071	0.1884	-15.5	-3.6	-12.3
KWAJ	2002	FO	0.2807	0.2621	0.2804	0.2744	-6.6	-0.1	-2.3
KWAJ	2003	FO	0.2379	0.2039	0.2431	0.2268	-14.3	2.2	-4.6
KWAJ	2004	FO	0.2269	0.174	0.1642	0.2027	-23.3	-27.6	-10.7
KWAJ	**1999-2004**	**FO**	**0.2383**	**0.2055**	**0.2194**	**0.2247**	**-13.7**	**-7.9**	**-5.7**

Table 3: Number of TRMM overpasses and associated TMI footprints available for this study over the period 1999-2004, for each GV site.

GV Site	*No. Overpasses*	*No. Footprints*			
		All	Ocean	Land	Coast
Kwajalein	257	70993	70993	0	0
Melbourne	236	54943	16875	16618	21450

Table 4 Melbourne regression parameters (A = All, O = Ocean, L = Land, C = Coast).

Satellite Product	TMI Surface Flag	RR Regime (mm/hr)	Regression Parameters		
			Intercept	R	Slope
TMI	A	0 - 20	1.44	0.99	0.40
PR	A	0 - 20	1.56	0.98	0.60
COM	A	0 - 20	1.19	1.00	0.68
TMI	O	0 - 20	2.32	0.98	0.40
PR	O	0 - 20	1.30	0.99	0.64
COM	O	0 - 20	1.12	0.99	0.63
TMI	L	0 - 20	1.53	0.98	0.47
PR	L	0 - 20	1.97	0.94	0.51
COM	L	0 - 20	1.35	0.97	0.84
TMI	C	0 - 20	1.37	0.99	0.58
PR	C	0 - 20	1.41	0.99	0.58
COM	C	0 - 20	1.14	1.00	0.70
TMI	A	21-40	6.21	0.69	0.27
PR	A	21-40	7.51	0.73	0.26
COM	A	21-40	4.48	0.86	0.62
TMI	O	21-40	6.93	0.36	0.18
PR	O	21-40	9.08	0.45	0.26
COM	O	21-40	-4.86	0.84	0.91
TMI	L	21-40	13.21	0.27	0.14
PR	L	21-40	12.36	0.11	0.05
COM	L	21-40	16.08	0.25	0.21
TMI	C	21-40	1.75	0.84	0.38
PR	C	21-40	2.97	0.78	0.43
COM	C	21-40	0.44	0.94	0.79

Table 5 Kwajalein regression parameters (all pixels are classified as ocean)

Satellite Product	TMI Surface Flag	RR Regime (mm/hr)	Regression Parameters		
			Intercept	R	Slope
TMI	O/A	0 - 20	1.65	0.97	0.46
PR	O/A	0 - 20	0.0	1.00	0.74
COM	O/A	0 - 20	0.39	1.00	0.61
TMI	O/A	21-40	4.37	0.78	0.25
PR	O/A	21-40	-4.50	0.91	0.87
COM	O/A	21-40	-17.12	0.92	1.32

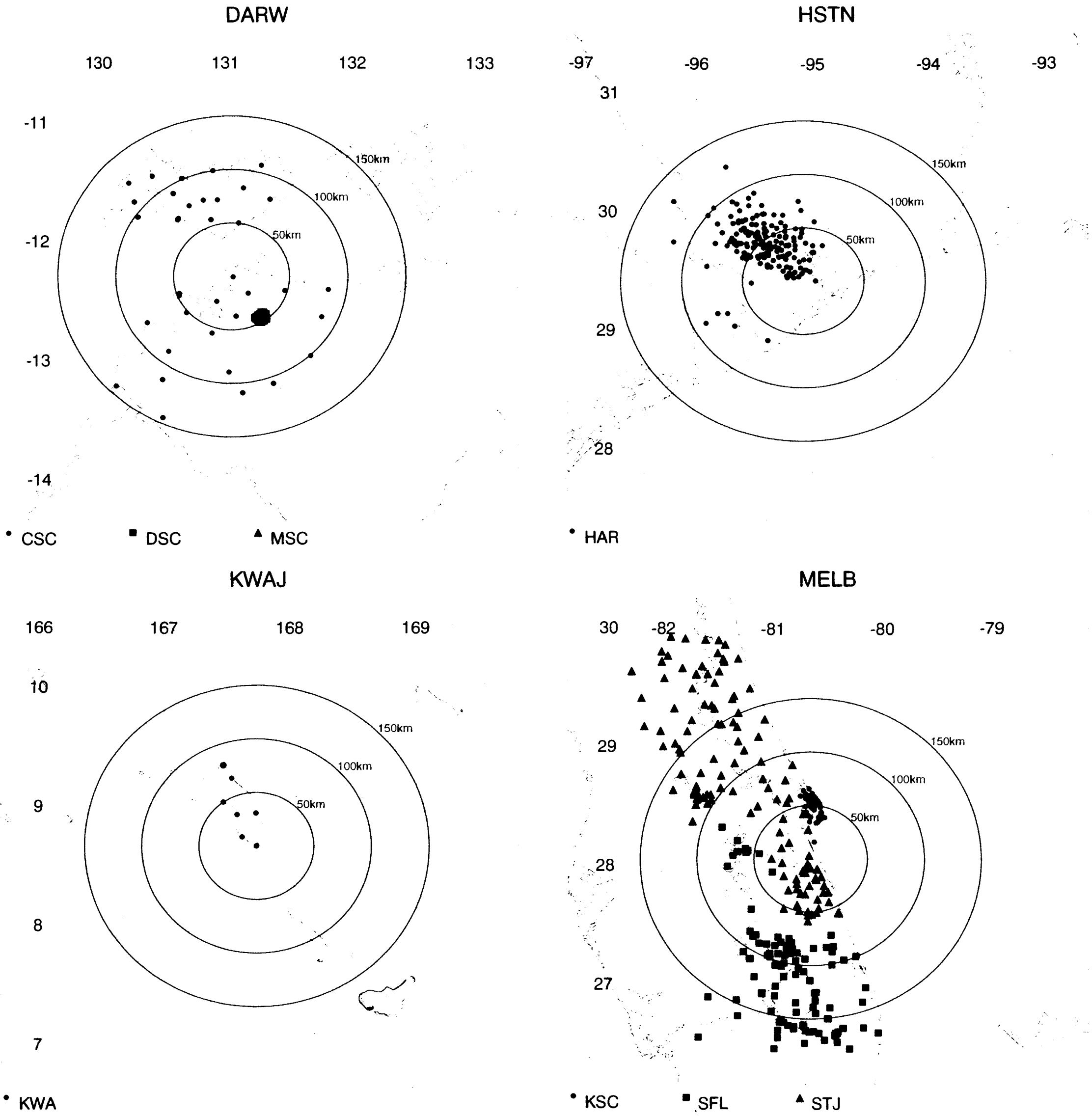

Fig. 1: Map illustrating the gauge and radar networks at GV sites: Darwin, Australia (DARW), Houston, Texas (HSTN), Kwajalein, Republic of the Marshall Islands (KWAJ) and Melbourne, Florida (MELB). Rings show distance from GV radar at increments of 50 km.

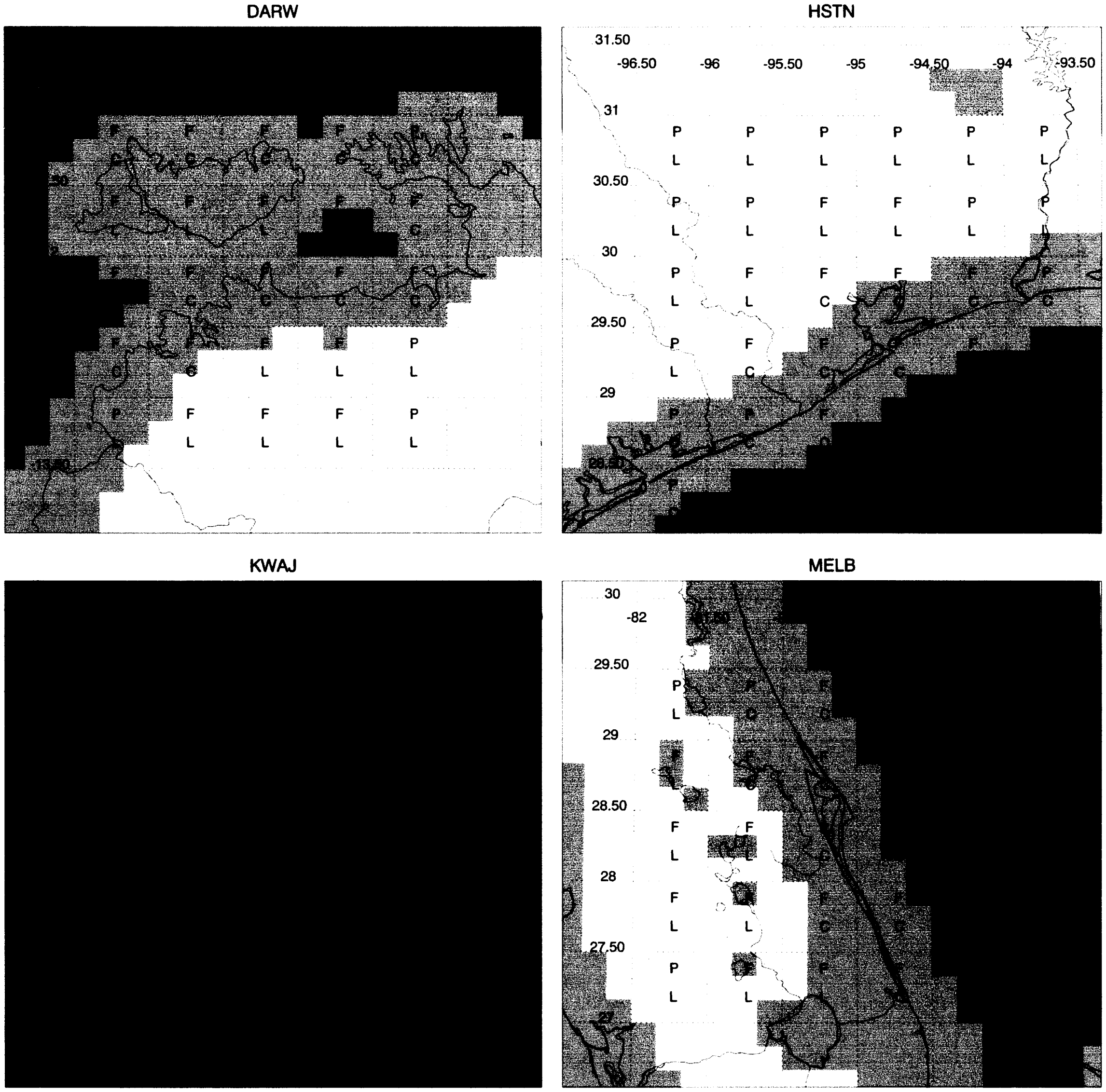

Fig. 2: Illustration of land/coast/ocean 1/6th degree mask used by the Version 6 TMI algorithm for each GV site. Shaded regions show TMI Version 6 surface mask of land (dark gray), coast (medium gray) and ocean (light gray). Also shown are the more subjectively classified 0.5° x 0.5° used for comparison of the GV data with the TRMM 3G68 product. The first letter designates the GV coverage (F denotes full GV coverage,

P is for partial), and the second letter designates the terrain-type: either (L) land, (C) coast, and (O) for ocean. Only areas with full GV coverage are used in this study.

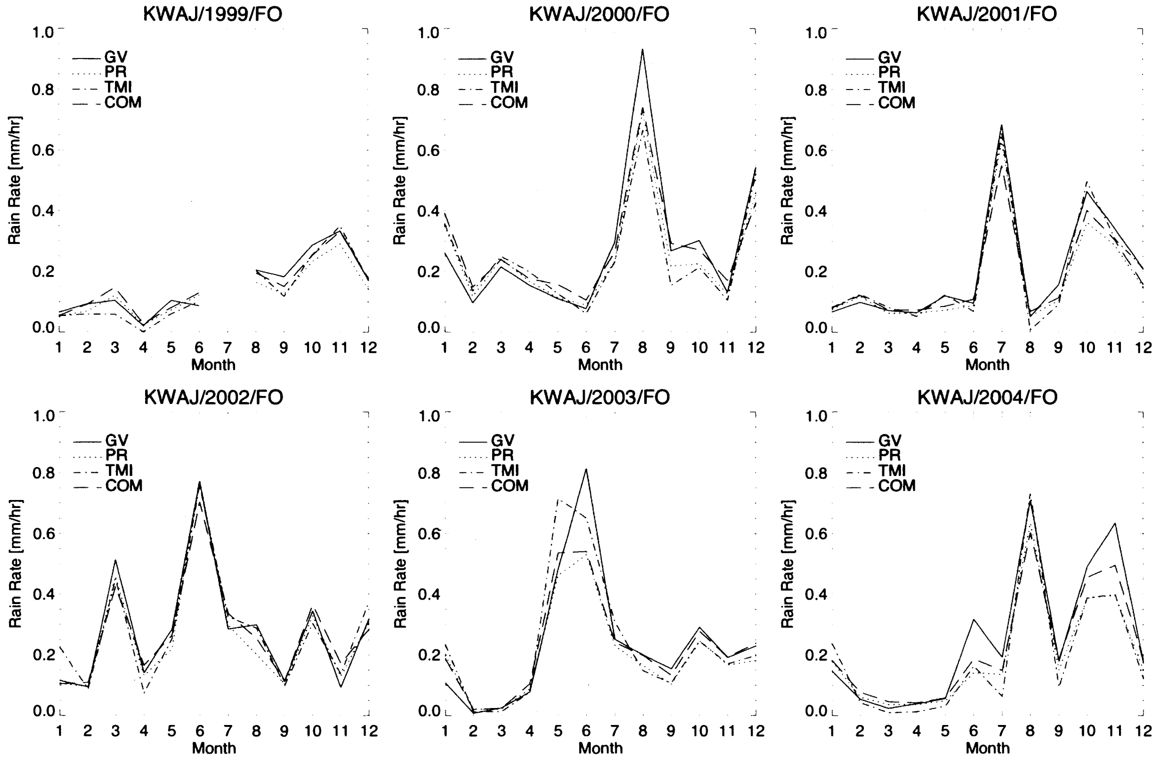

Fig. 3: Mean monthly rain intensities (mm/hr) for GV (solid), PR (dot), COM (dash-dot) and TMI (dash) using 0.5° resolution for the period 1999-2004 at KWAJ.

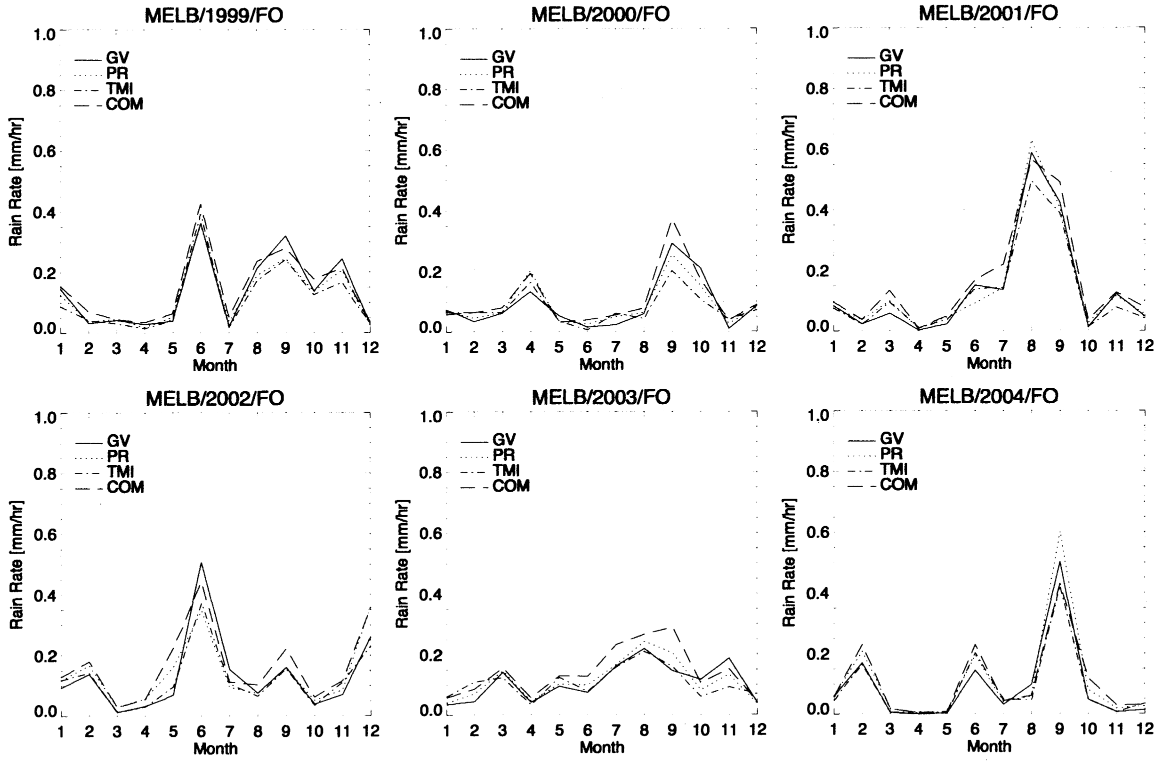

Fig. 4: Same as Fig. 3, except for MELB (ocean only).

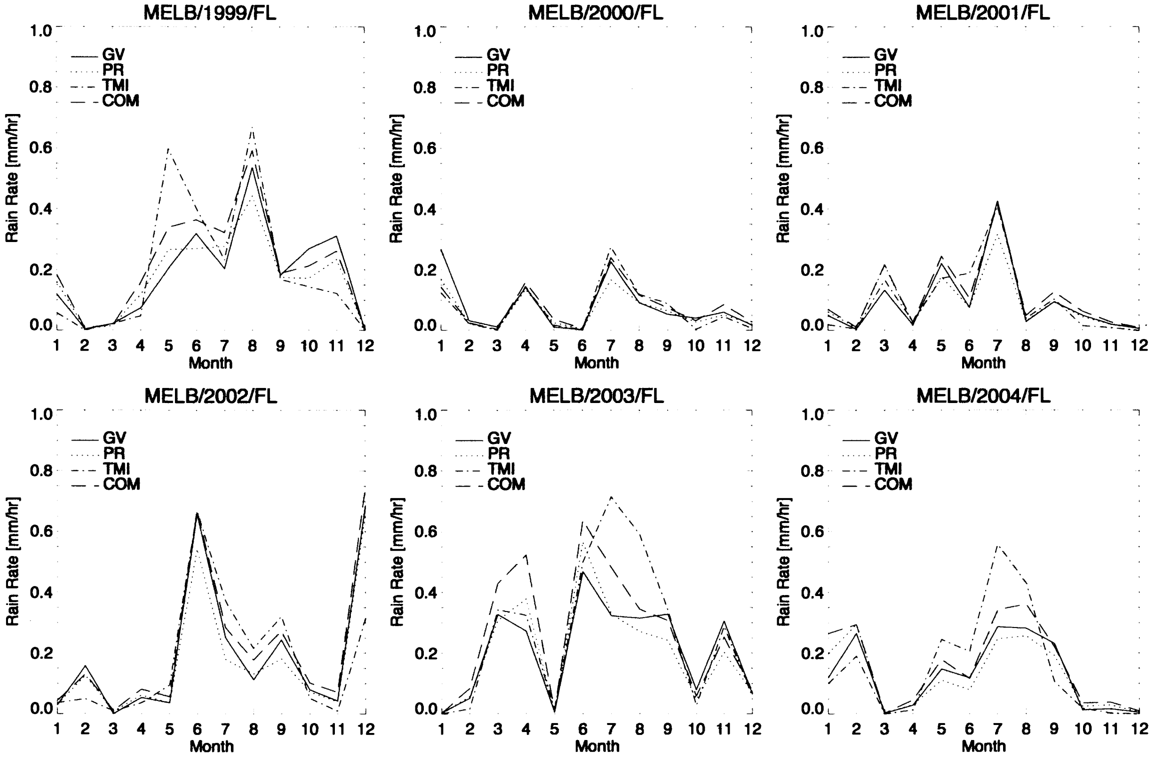

Fig. 5: Same as Fig. 3, except for MELB over land only.

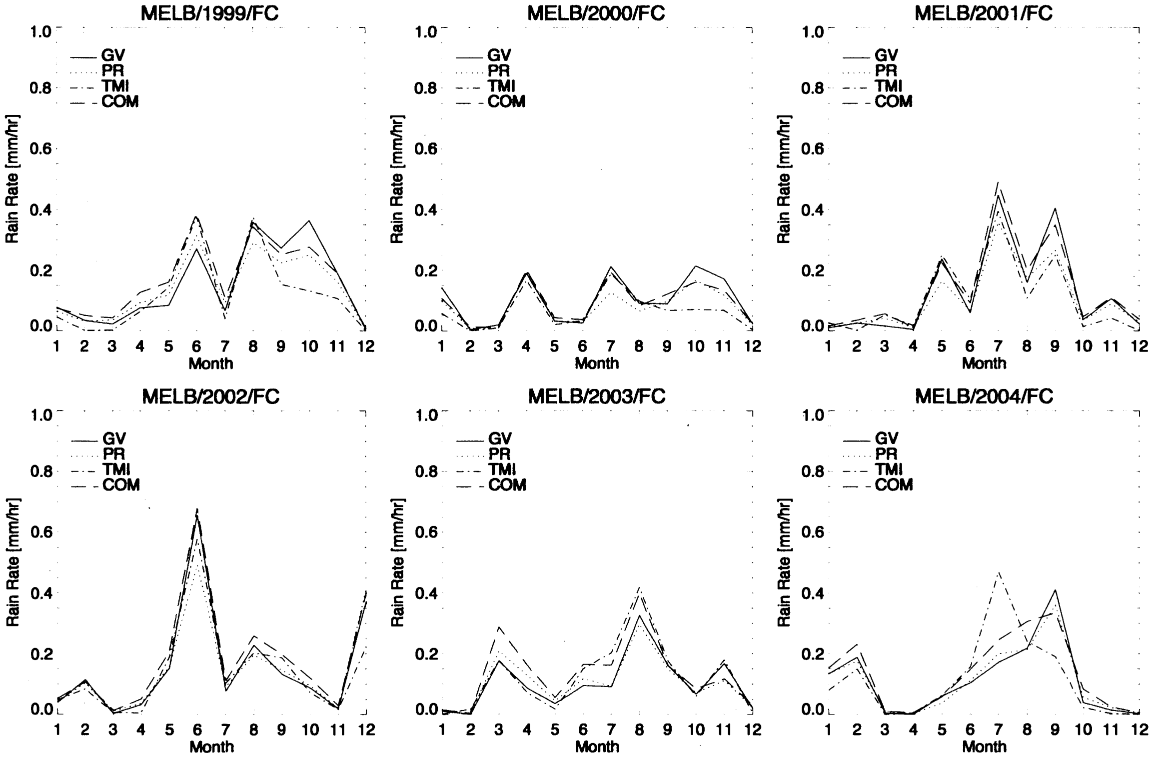

Fig. 6: Same as Fig. 3, except for MELB over coast only.

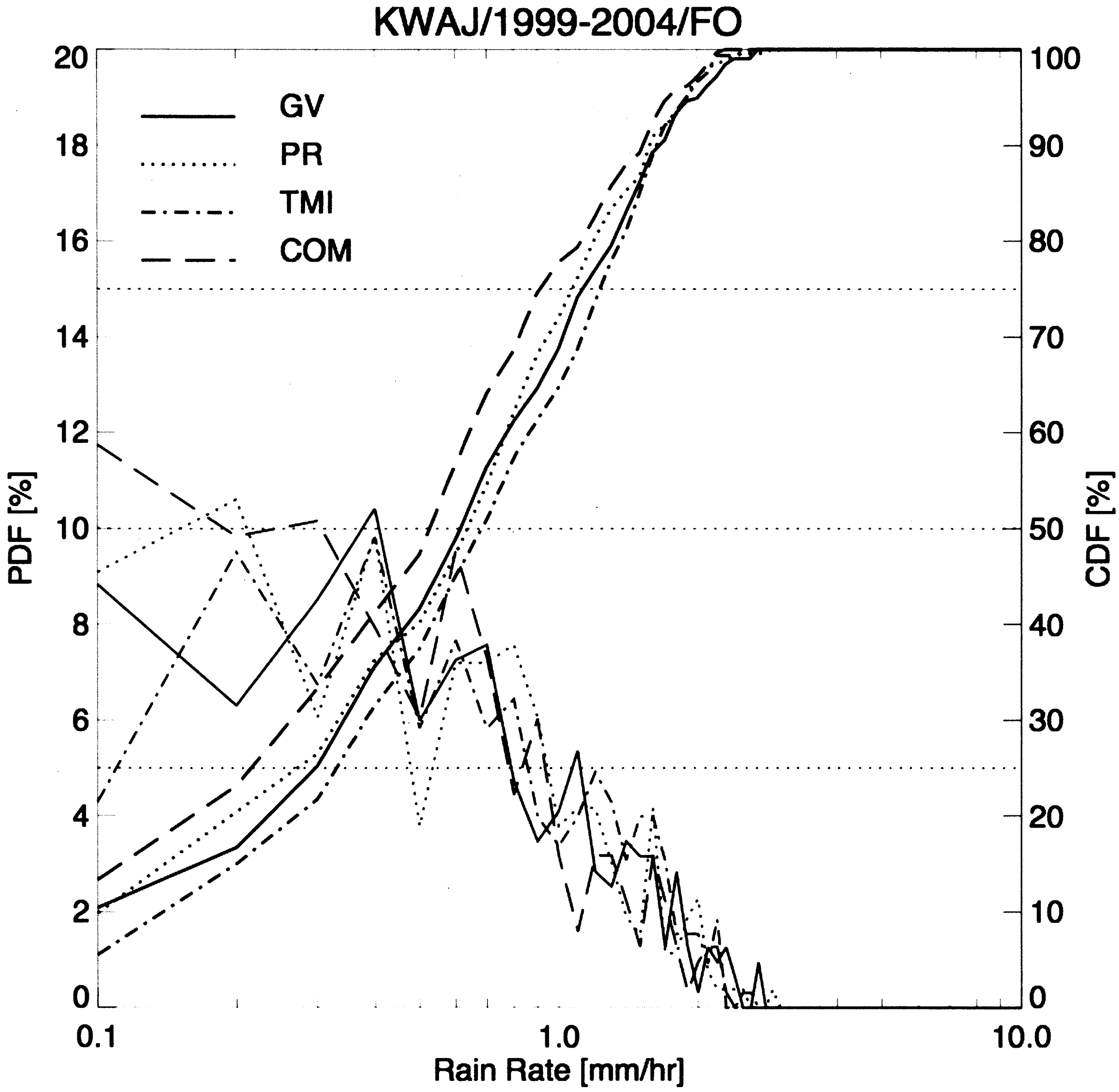

Fig. 7: Probability Density Function (PDF) and Cumulative Distribution Frequency (CDF) of instantaneous rain rates (0.5° resolution) for GV (solid), PR (dot), COM (dash-dot) and TMI (dash) as inferred from 3G68 products using 0.5° resolution for the period 1999-2004 at KWAJ.

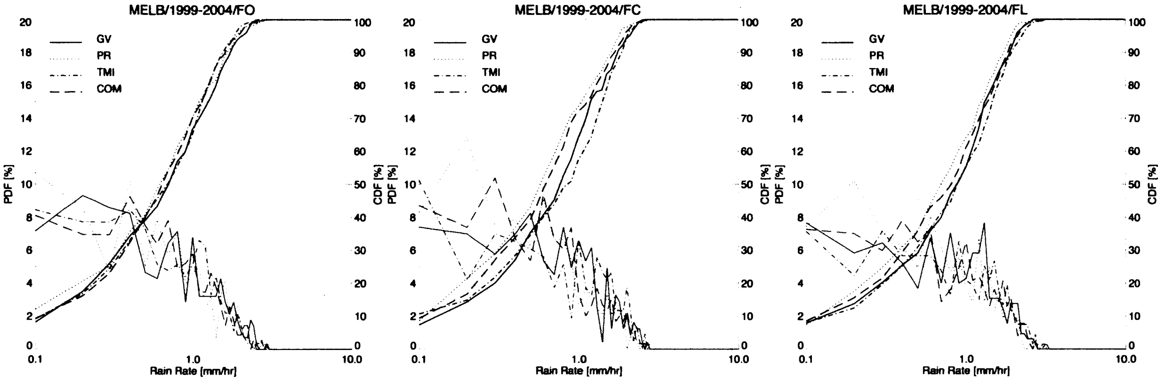

Fig 8: Same as Fig. 7, except for MELB over ocean (left panel), coast (middle panel) and land (right panel).

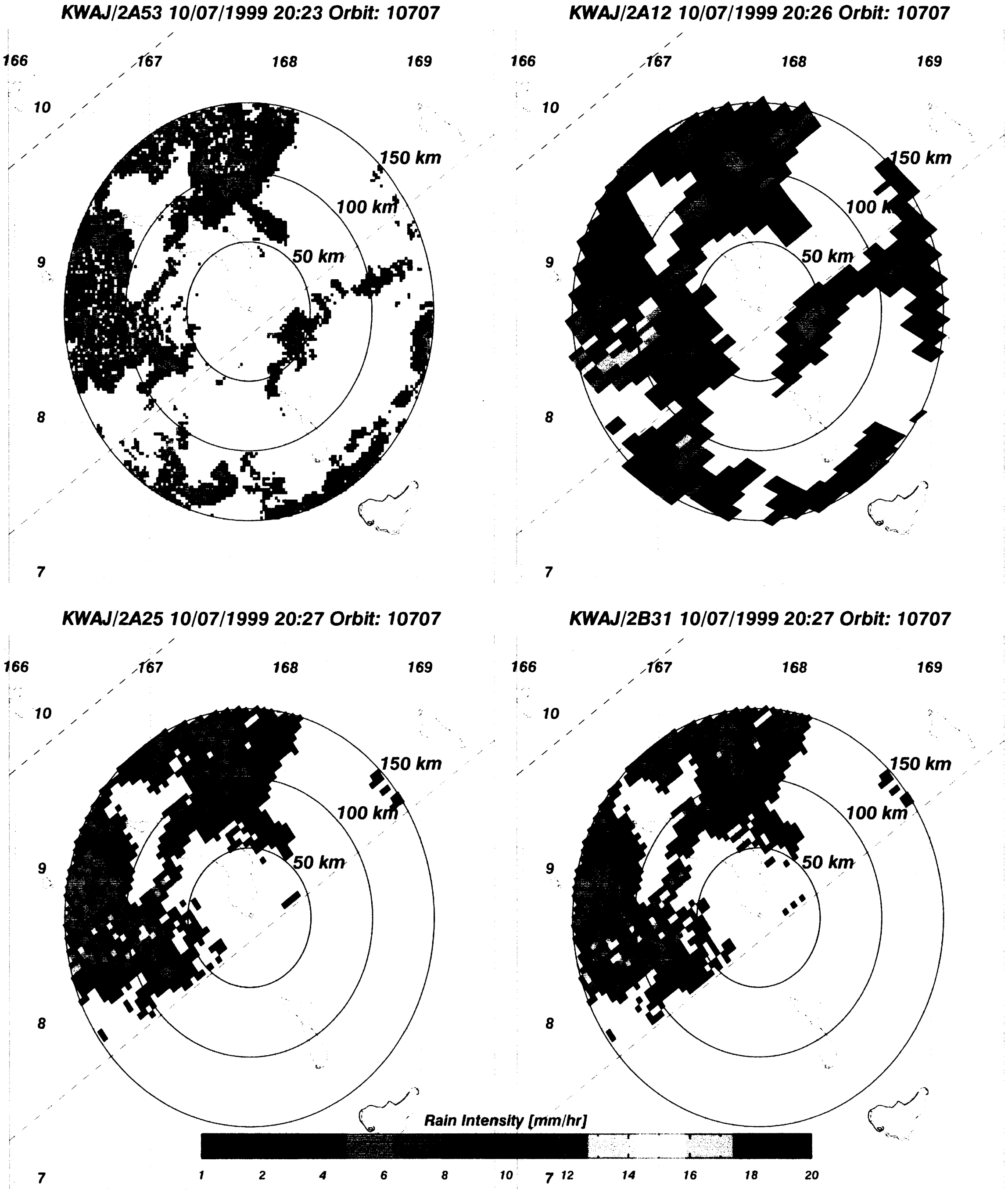

Fig. 9: Illustration of a TRMM overpass of the KWAJ GV sites on 10/07/1999 showing the Level II rain data at each instrument's native resolution: top left panel (GV 2 km x 2

km; top right panel (TMI ~150 km^2 resolution); bottom left panel (PR 4 km at nadir); and bottom right panel (COM 4 km at nadir).

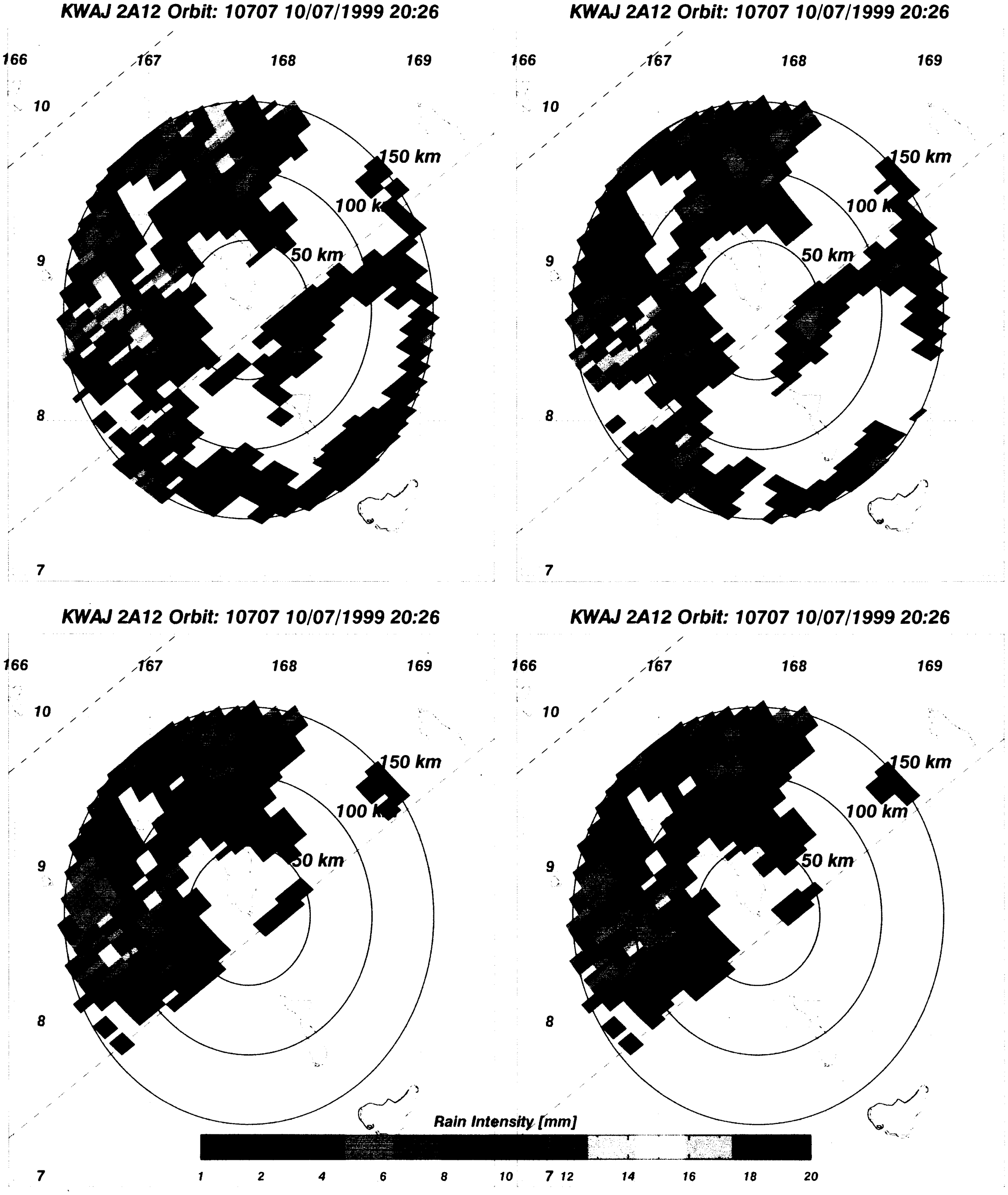

Fig. 10: Same as Fig. 9, except the GV, PR and COM data have been averaged within each TMI footprint.

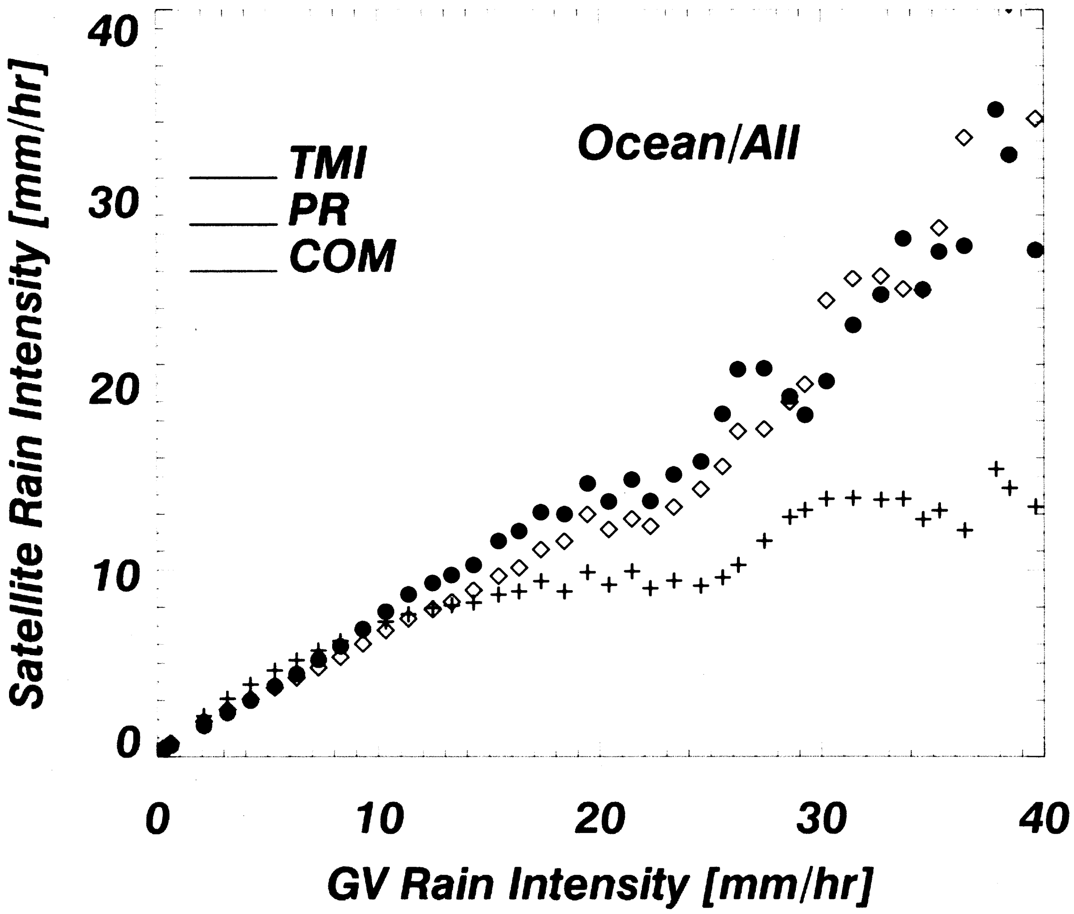

Fig. 11: Scatter diagram of TMI (black), PR (blue) and COM (red) mean rain intensities versus mean rain intensities of the GV radar at Kwajalein.

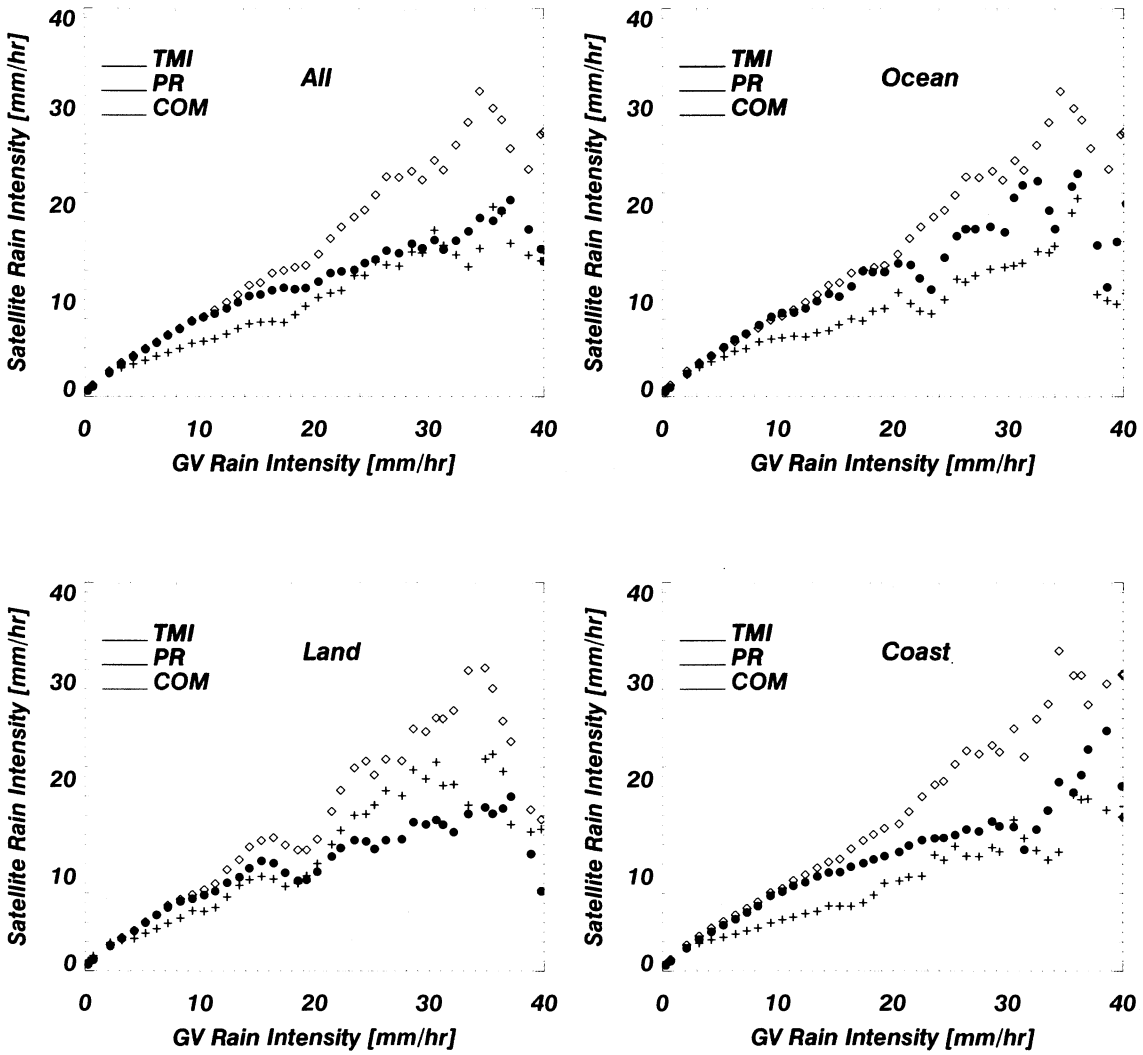

Fig. 12: Scatter diagrams of TMI (black), PR (blue) and COM (red) mean rain intensities versus mean rain intensities of the GV radar at Melbourne. The four panels show rain rate profiles for: (top left) all matched data points; (top right) Ocean only; (bottom left) Land only; (bottom right) Coast only.

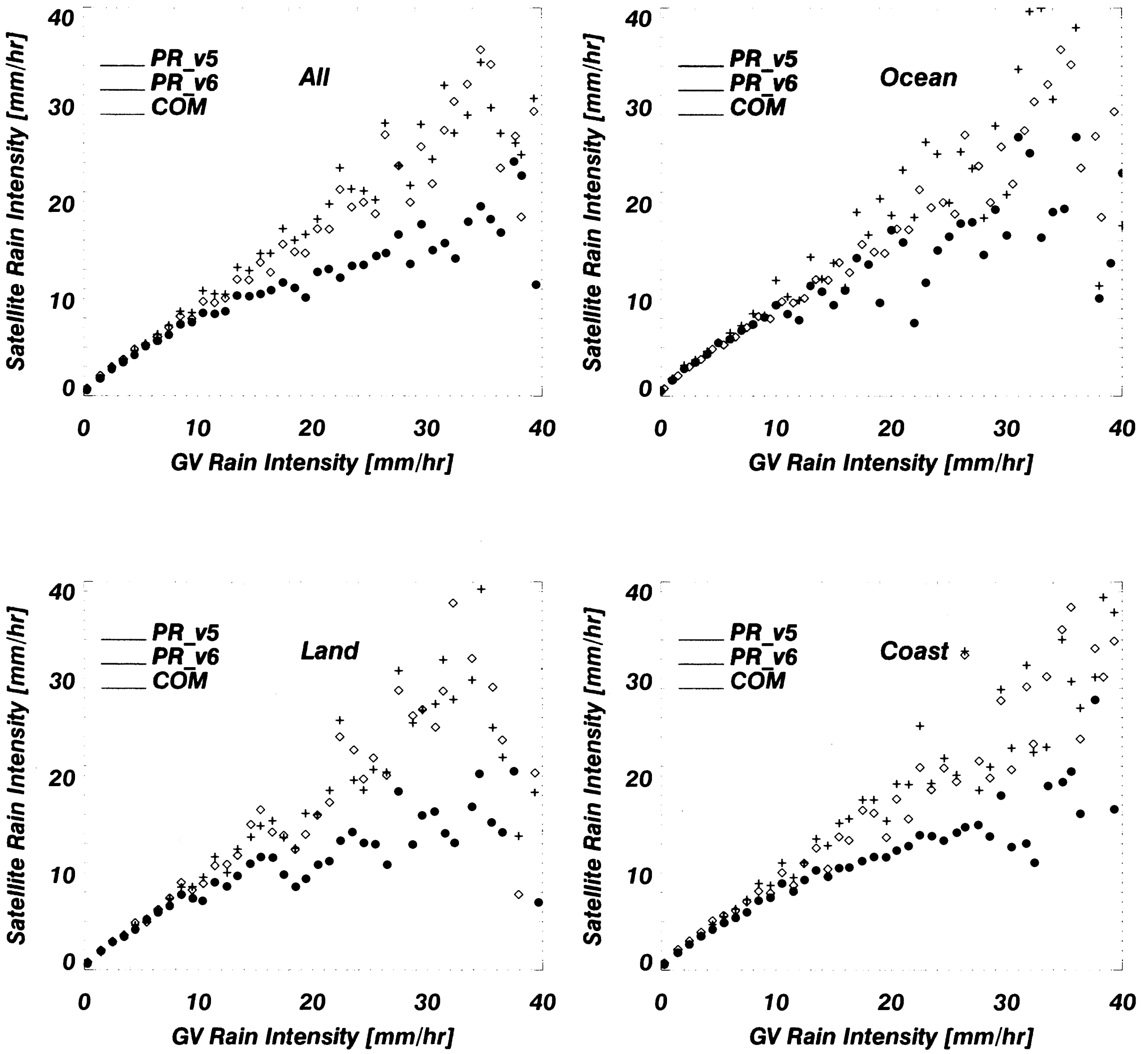

Fig. 13: Scatter diagrams based on 150 good overpasses of GV site at Melbourne showing rain rate profiles for PR (version 5), PR (version 6) and COM.

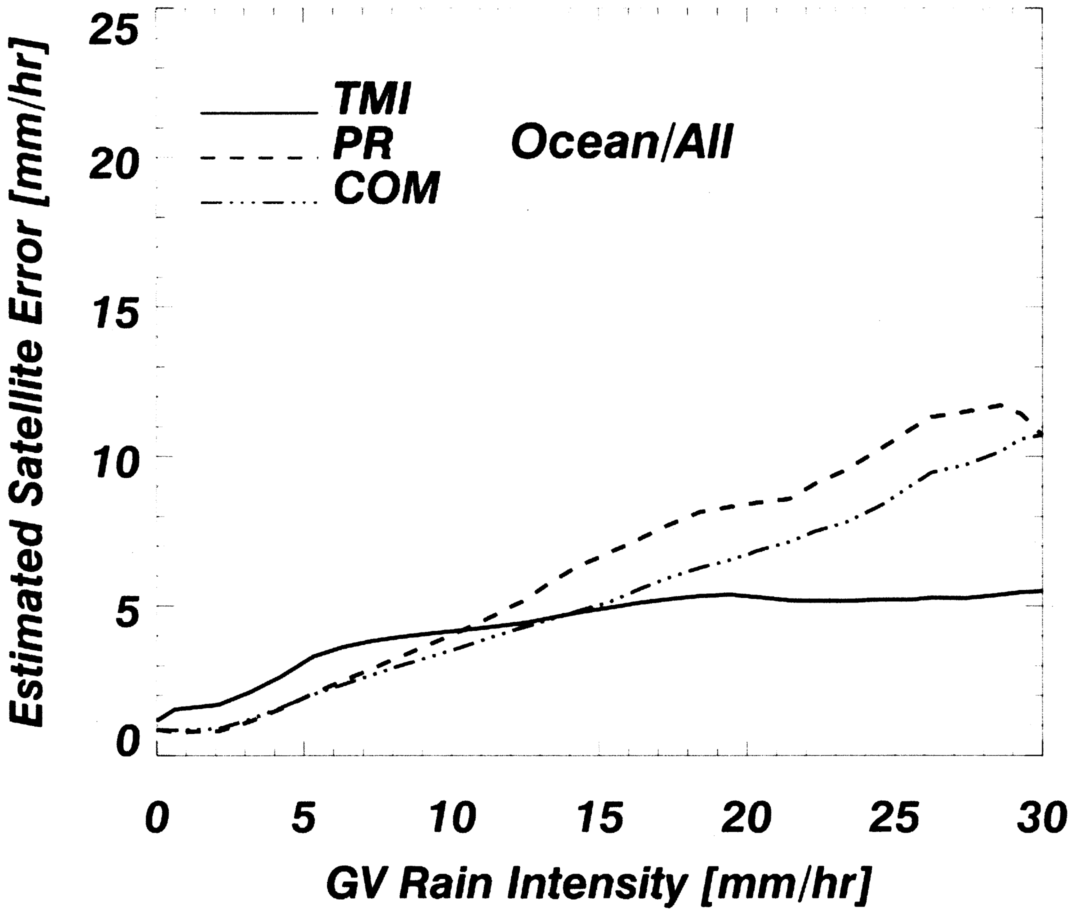

Fig 14: Profile displays the standard errors for the TMI, PR and COM at KWAJ versus the GV rain rate intensity. Errors were determined based on the variance difference between the matched satellite rain rates and the GV radar at Kwajalein.

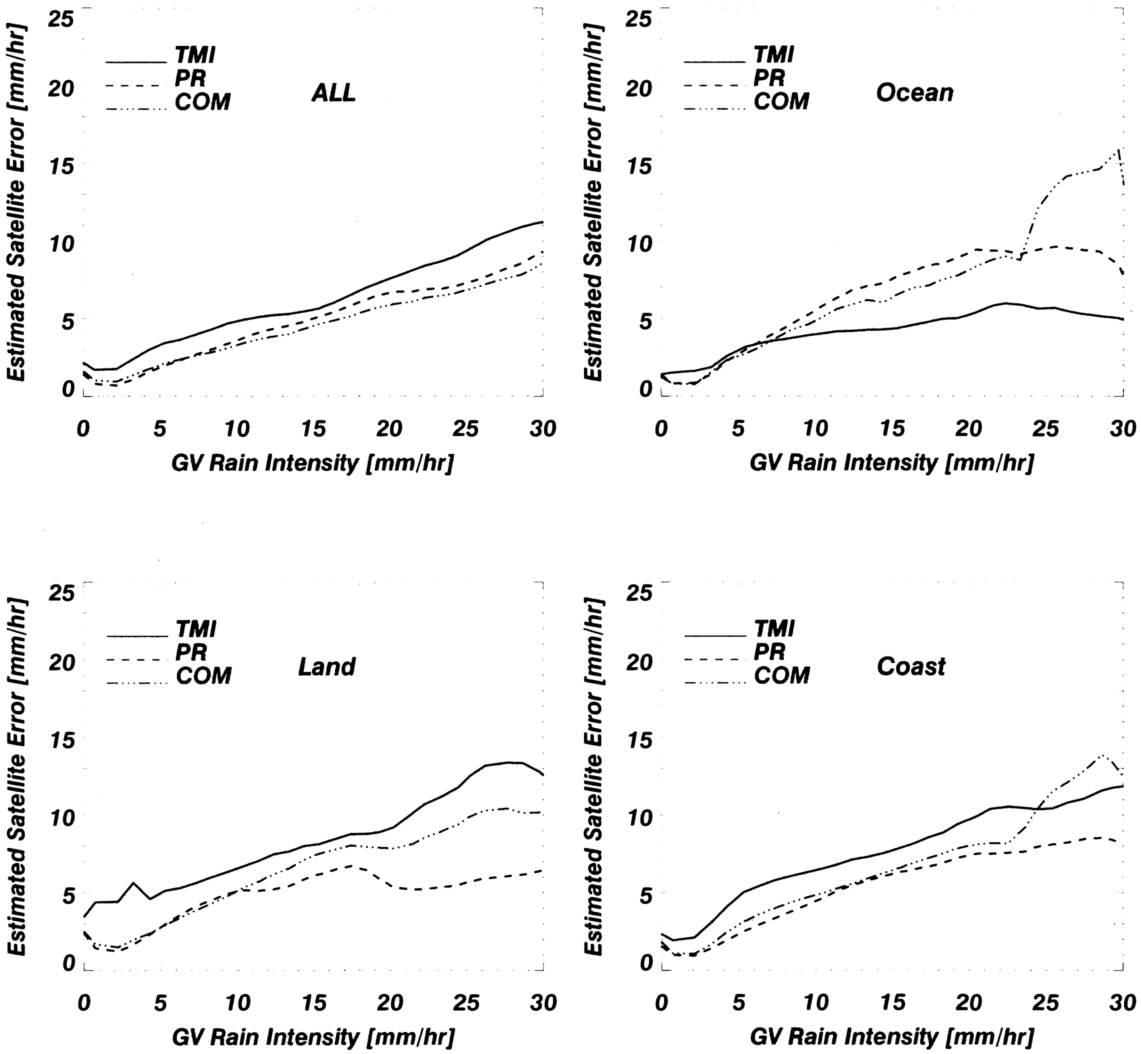

Fig. 15: Profile displays the standard errors for the TMI, PR and COM at MELB versus the GV rain rate intensity. The four panels show results for: (top left) all matched data points; (top right) Ocean only; (bottom left) Land only; (bottom right) Coast only.

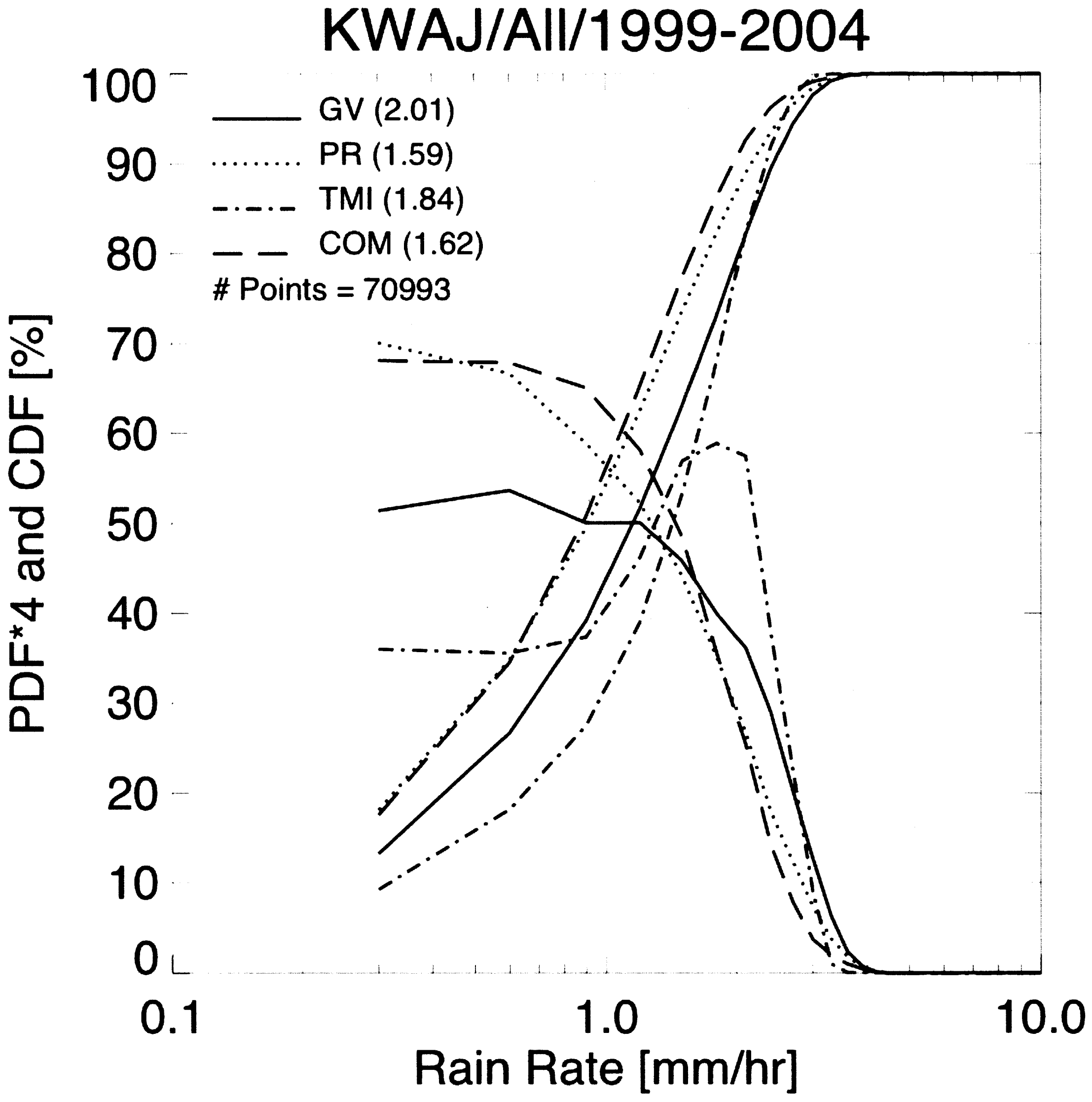

Fig. 16: PDF and CDF of rain rates for GV (solid), PR (dot), COM (dash-dot) and TMI (dash) estimates using 0.5° resolution for the period 1999-2004 at KWAJ at the TMI footprint scale.

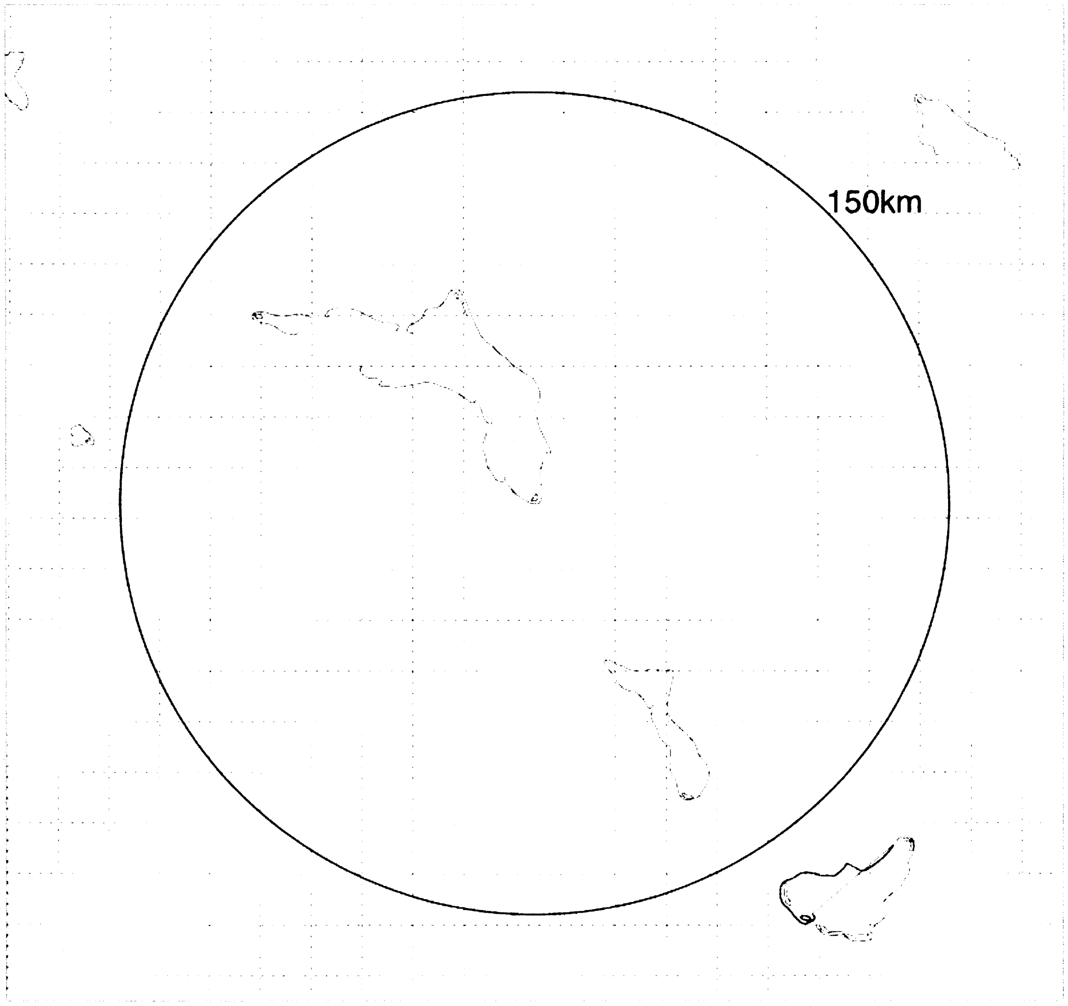

Fig. 17: Sub-setted classification of KWAJ using a rough estimate of the TMI Version 5 surface mask, which considered the areas near the atolls to be coastal.

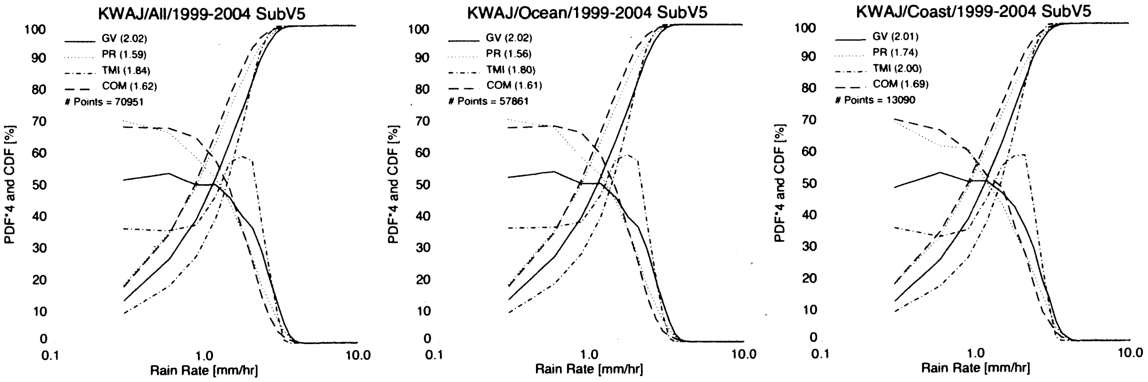

Fig. 18: PDF and CDF rain rates at KWAJ over gray area shown in Fig. 17 (top left panel), white area in Fig. 17 (middle panel) and all areas (same as in Fig. 16).

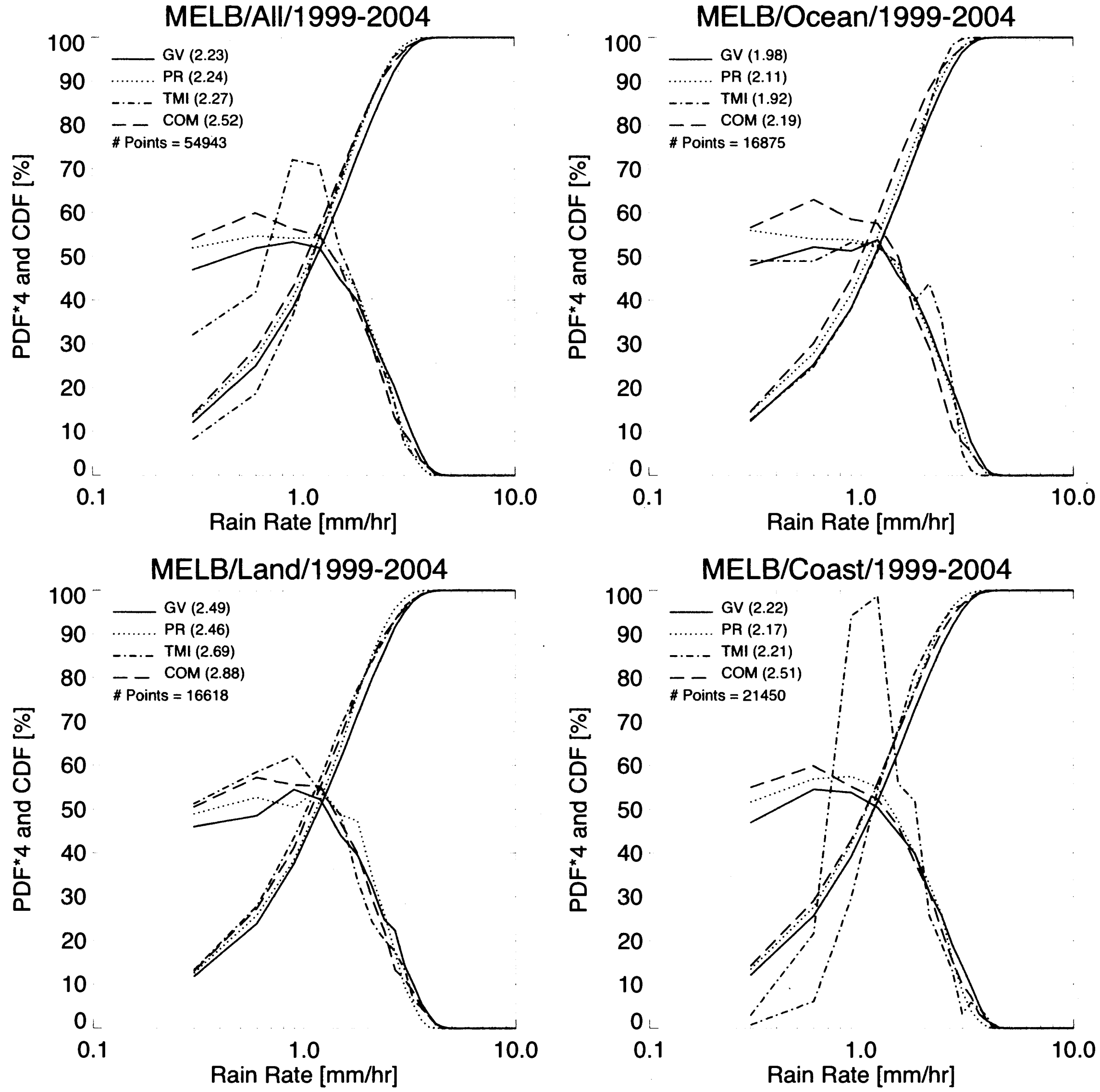

Fig. 20: PDF and CDF of rain rates at MELB at the TMI footprint scale for the period 1999-2004 showing GV (solid), PR (dot), COM (dash-dot) and TMI (dash). Top left panel shows the full GV area; top right panel is for ocean areas only; bottom left panel is for land areas only, and the bottom right is for coastal areas only.